UNIVERSITY OF NOVA GORICA
SCHOOL OF APPLIED SCIENCES

SIMULATION OF MICRO BLACK HOLE EVAPORATION AND INTERACTION IN THE EARTH'S ATMOSPHERE

MASTER'S THESIS

Gašper Kukec Mezek

Mentor: prof. dr. Danilo Zavrtanik

Nova Gorica, 2014

Acknowledgments

A big thanks goes to Danilo Zavrtanik and Samo Stanič for their help and guidance concerning this thesis. I would also like to thank Maria Vittoria Garzelli and Ruben Conceição for their help with Monte Carlo simulators that we used. Lastly, the support from family and friends kept me going and I thank them for it.

Povzetek

Pri trkih delcev z energijo nad Planckovo skalo in s parametrom trka manjšim od dvakratne vrednosti horizontnega polmera, lahko nastane semiklasična mikroskopska črna luknja (μBH). Planckove skale (10^{19} GeV) danes pri trkih ni mogoče doseči, prvobitne μBH, ki bi lahko nastale v Velikem poku, pa so že razpadle. V primeru veljavnosti višjedimenzionalnih modelov prostora-časa se energija za tvorbo μBH spusti do energij reda velikosti nekaj TeV, ki so dosegljive tako pri trkih v velikem hadronskem trkalniku (LHC) v raziskovalnem centru CERN, kot tudi pri trkih kozmičnih žarkov ekstremnih energij (UHECR) z jedri atomov zraka v Zemeljski atmosferi. Pri meritvah trkov proton-proton s težiščno energijo do 7 TeV, ki jih izvajata kolaboraciji ATLAS in CMS na trkalniku LHC, nastanka μBH niso opazili, zato bodo meritve ponovili pri končni, podvojeni težiščni energiji trkalnika. Alternativen način detekcije μBH preko trkov kozmičnih žarkov ekstremnih energij dosega do štiridesetkrat višje težiščne energije, kot bodo dosegljive v LHC. Primarno interakcijo moramo v tem primeru identificirati preko obširnega atmosferskega plazu sekundarnih delcev, ki ga detektiramo z detektorskimi sklopi observatorija Pierre Auger. Kljub ekstremnim energijam, ki jih UHECR dosegajo, je ta način študija μBH omejen z majhnimi fluksi kozmičnih žarkov pri najvišjih energijah in posledično z nizko statistiko, ki otežuje razločevanje med atmosferskimi plazovi z različno začetno interakcijo.
V sklopu tega dela smo proučili možnost razločevanja atmosferskih plazov, ki izvirajo iz razpada μBH, od plazov, ki so posledica interakcij UHECR z jedri atomov zraka, predvsem interakcij proton-proton in Fe-proton. Opravili smo simulacije tvorbe in razpada μBH na nivoju partonskih pljuskov, kot tudi nadaljne hadronizacije in razvoja plazu sekundarnih delcev. Simulacije smo izvedli z združitvijo Monte Carlo simulatorja tvorbe in razpada μBH (BlackMax) s paketom za opis hadronizacije (PYTHIA) in simulacijo razvoja atmosferskih plazov sekundarnih delcev (CORSIKA).

Ključne besede: astrofizika osnovnih delcev, kozmični žarki ekstremnih energij, mikroskopske črne luknje, obširni atmosferski plaz sekundarnih delcev, simulacije Monte Carlo, dodatne dimenzije
PACS: 04.70.Dy, 04.50.Gh, 96.50.sd

Abstract

A semi–classical micro black hole (μBH) can be created in particle collisions with energies exceeding the Planck scale and an impact parameter smaller than twice its horizon radius. Such high energy, of the order of 10^{19} GeV, could only have been achieved right after the Big Bang, making it impossible to distinguish any of their decay products at the present day. However extra–dimensional theories foresee a plausible diminishment of the production energy down to energies at the TeV level, which are accessible to the Large Hadron Collider (LHC) at CERN and even more so to experiments studying ultra–high–energy cosmic rays (UHECR). Searches for μBHs have already been performed by ATLAS and CMS collaborations at LHC, with negative results on their existence. Further searches will be carried out in the near future, when the LHC energy will be upgraded to twice its present value. UHECR detectors, like the Pierre Auger Observatory, are sensitive to cosmic ray particles with energies exceeding $E_0 = 10^{19}$ eV (~130 TeV in center–of–mass of a p–p collision) and are possible places to look for μBH creation. However, the low flux of UHECR at extreme energies and the consequent low statistics could largely hinder observations of μBH induced showers.
To investigate if μBH induced extensive air showers (EAS) can be distinguished from normal showers started by a primary particle, we performed simulations of μBH production and decay as well as EAS evolution processes. The former was done using a coupling of BlackMax micro black hole event generator and PYTHIA hadronization software, whereas the latter incorporated the use of EAS simulator CORSIKA.

Keywords: astroparticle physics, ultra–high–energy cosmic rays, micro black holes, extensive air showers, Monte Carlo simulations, extra dimensions
PACS: 04.70.Dy, 04.50.Gh, 96.50.sd

Contents

1 Introduction

Particle physics and astroparticle physics have provided us with larger and more detailed insights into the makings of matter surrounding us since the beginning of the previous century. While the latter is limited on the study of particles from extraterrestrial sources with sporadic occurrences, particle physics delves deeper into the structure of matter, uncovering exotic particles that might shed light on many as of yet unconfirmed theories, for example strings or micro black holes. Therefore, it has overshadowed astroparticle physics due to a greater collision rate with high statistics and far superior containment of the interaction point, surrounding it with various detectors. However, with most of the processes that aim to discover particles with higher mass, weakly interactive particles or interactions at better spatial resolutions, the demand for high energy particle collisions has been steadily increasing. Although there is an upgrade of the large hadron collider (LHC) in progress for collisions up to 14 TeV, it already seems that we are looking for alternatives that might exceed the limitations of current operational accelerators and colliders. It turns out that cosmic rays are the alternative, because their collisions with the Earth's atmosphere have been measured with a center–of–mass energy more than 30 times larger than that of the LHC. With some of the focus again on astroparticle physics, new detector systems are being developed, aiming at determining the identity of cosmic rays, their interactions, origins and the acceleration processes that causes them to accelerate to such colossal energies.
Micro black holes are black holes that have a mass 1000 times larger than that of a proton compacted into an extremely small space, below the Planck limit of $\sim 10^{-35}$ m. They supposedly existed in the short time after the Big Bang, when all four fundamental forces were unified, making them impossible to detect now, almost 14 billion years after the Big Bang. However, assuming that there are extra dimensions, apart from the 4–dimensional space–time, might lower the energy needed to create a micro black hole to energies reachable by man–made accelerators. The search for micro black holes is being performed at the LHC, looking for signature emissions of particles when a micro black hole evaporates. With the currently gathered data, there has been no indication such objects exist, thus it appears that higher energy collisions are needed to detect them. Therefore, UHECR could be a better choice for their detection through the cascade of secondary particles created in the atmosphere. A viable concern is the resolution and accuracy of air shower detectors, when it comes to distinguishing possible micro back hole induced cascades to cascades resulting from other particle types.
In light of determining the probability of micro black hole detection, the scope of this thesis is to connect simulation processes of micro black hole production, hadronization and extensive air shower creation, by linking the Monte Carlo simulators, BlackMax, PYTHIA and CORSIKA. Each of these handles one of the two mentioned processes, but by combining them we can follow a micro black hole from its production in a cosmic ray collision, through its decay to the creation of an extensive air shower from the emitted particles.
Chapters 2 and 3 give a general introduction into cosmic rays and micro black

holes, followed by the description of the complete simulation setup adopted for this work in chapter 4. The final two chapters hold results obtained from simulations (chapter 5) and conclusions with future prospects (chapter 6). Due to the large energy range of air shower particles and the necessary conversion between center–of–mass and laboratory frame energies, it was rather difficult to select constant unit prefixes for energy, therefore Appendix A gives fast comparison and conversion factors, along with constants used in equations. Appendix B lists common particle codes used in both simulation programs.

2 Ultra–high–energy cosmic rays

Part of the background radiation that we are exposed to every day, consists of particles coming from extraterrestrial sources. These incident particles are known as cosmic rays (CR) and can be composed of various particle types, such as protons, electrons, photons and other nuclei originating from stars or other violent processes in the Universe. The energy range of cosmic rays is vast, from particles barely breaking the top of Earth's atmosphere, to those that induce a large cascade of particles after interacting with air molecules in the atmosphere. However, cosmic rays from opposite sides of the energy range differ in another characteristic. Low energy cosmic rays are plentiful, making their detection simple, as long as we can setup experiments on satellites or high–altitude weather balloons, whereas high energy cosmic rays arrive to Earth from distant sources extremely rarely. A simple way of explaining this is through an energy spectrum of cosmic rays, obtained through numerous experiments, shown on figure 2.1. The vertical axis displays

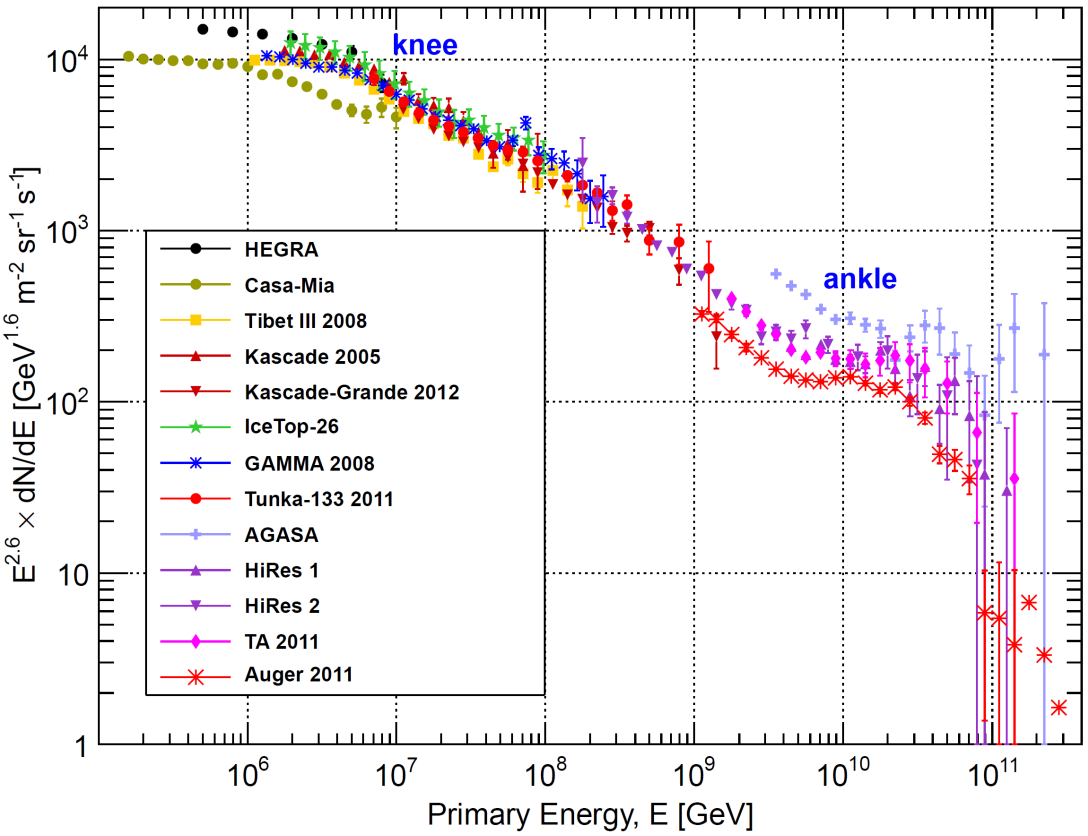

Figure 2.1: Cosmic ray spectrum including various air shower experiments. The flux $F = \frac{dN}{dE}$ on the vertical axis is multiplied by $E^{2.6}$ in order for spectrum features (knee, second knee and ankle) to be more visible (figure ref. [1]).

the flux of cosmic rays $F = \frac{dN}{dE}$, that is the number of particles per unit area per unit time, cleverly multiplied by a factor of $E^{2.6}$ in order for characteristics of the spectrum to show more clearly. Inflections visible on the spectrum are the so called

knee and *ankle*. The first marks a shift between sources inside our solar system and galactic sources of cosmic radiation. It is also around this region that satellite or balloon measurements are no longer profitable due to an increasingly smaller flux of particles. The other feature is called *ankle*, contributed to the change between galactic and extragalactic sources of cosmic rays. As an example of the frequency of incident cosmic rays, when observing particles from the *knee* region, we encounter around one particle per square meter per second, while rare cosmic rays from the *ankle* region reach the same area roughly once per year. It is therefore quite apparent why properties of high–energy cosmic rays still elude us. Venturing even beyond the *ankle*, there is an apparent abrupt stop to cosmic rays. The exact nature of this cut–off could be due to the GZK (Greisen–Zatsepin–Kuzmin) effect or a reduction of CR sources at extreme energies. The GZK (Greisen–Zatsepin–Kuzmin) effect describes the loss of energy of cosmic rays through interactions with the cosmic microwave background radiation (CMB), thus forming pions:

$$\begin{aligned} p + \gamma_{\mathrm{CMB}} &\longrightarrow p + \pi^0, \\ &\longrightarrow n + \pi^+. \end{aligned}$$

This lowers the CR energy under the pion production limit of $\approx 50\,\mathrm{EeV}$, creating a sudden drop in the spectrum. The GZK effect is still under debate, because large surface arrays have recorded events above the proposed limiting energy, with any further occurrences at such high energies appearing only once per square kilometer per year (in extreme cases even per century). More on the properties of the cosmic ray spectrum can be found in [1].
Despite the low flux, cosmic rays with extreme energies are being thoroughly investigated for their unknown acceleration source that propels them to energies unreachable at man–made accelerators. When carrying energies above $\sim 10^{18}\,\mathrm{eV}$, we commonly name them as ultra–high energy cosmic rays (UHECR) and by comparing them with the large hadron collider (LHC), they possess more than 30 times the collision energy of $\sqrt{s_{\mathrm{LHC}}} = 14\,\mathrm{TeV}$ which will be reached at the LHC in the next few years. Unfortunately, not much is known about the composition of UHECRs, since direct detection is impossible, as they require a large detector volume to obtain enough information on their properties (direction, energy, type). The most practical way of observing them at the moment is by considering the Earth's atmosphere as one large calorimeter, creating an enormous cascade of particles known as an extensive air shower (EAS). From the measured air shower signal we can consequently obtain energy, arrival direction and information on mass of the primary particle.

2.1 Extensive air showers

The formation of an EAS occurs when a high–energy cosmic ray enters the Earth's atmosphere, interacts with air molecules, thereon producing multiple secondary particles. In the case of a hadronic shower, these secondary particles are most commonly barions and mesons, out of which the majority are pions ($\pi^{\pm}$, π^0). They in turn interact with air molecules or decay and produce even more particles. Barions continue the hadronic part of the cascade, while pions start the electromagnetic part through decay channels $\pi^0 \longrightarrow 2\gamma$, $\pi^- \longrightarrow \mu^- \overline{\nu}_\mu$ and

$\pi^+ \longrightarrow \mu^+ \nu_\mu$. A simple scheme of the beginning of such a shower is displayed on figure 2.2. Opposed to hadronic, an electromagnetic shower is just what you would

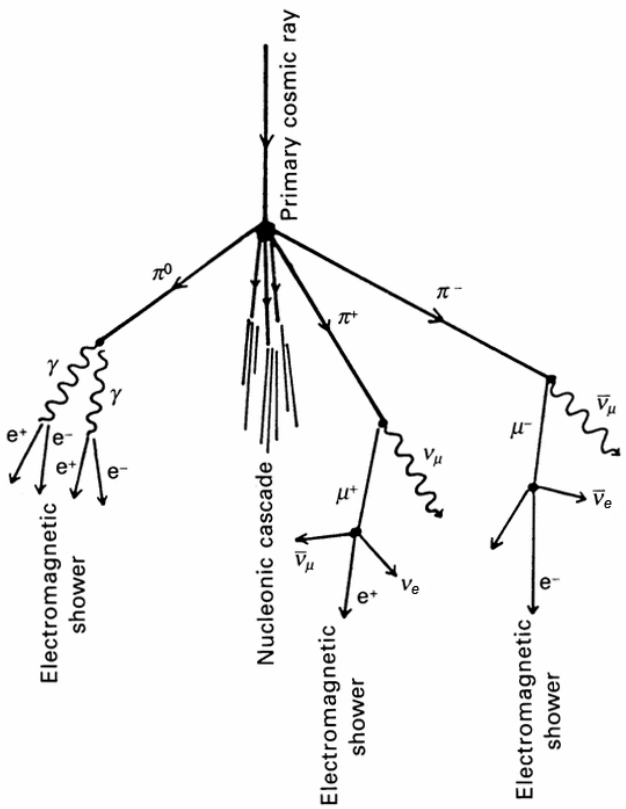

Figure 2.2: A schematic view of a hadronic EAS formation. After an interaction between the primary cosmic ray and an air molecule, secondaries are produced, that later interact with the atmosphere again or decay (figure ref. [2]).

expect from its name. It starts off with a primary photon, electron or positron that, having a small cross–section for hadron production, mainly produces electromagnetic particles. The hadronic part of such a cascade is thus almost negligible. No matter what kind of EAS we have, particles will lose energy when traveling through the atmosphere, either due to collisions and decays that produce particles with lower energies than the starting particle or due to bremsstrahlung radiation. At some point the energies of shower particles gets low enough for bremsstrahlung to overwhelm new particle production, decreasing the amount of particles in a shower. The peak, where an EAS has a maximal number of particles, is named the shower maximum $X_{\max}$ and gives a representation on how different types of particles are interacting in a shower. For instance, hadrons will reach their maximum the fastest and we therefore barely observe any at ground level. The amount of electromagnetic channels for $e^\pm$ and photons ensures them that they reach the shower maximum deeper in the atmosphere and will be observed with ground detectors. Lastly, muonic shower components tend to be very durable, since muons lose less energy through bremsstrahlung radiation than electrons and travel at speeds large enough to survive to ground level due to relativistic time dilation. Remaining neutral particles are far harder to detect, because we need to be aware of their decay and interaction processes, which is tedious at best. In most obser-

vatories they are therefore treated as missing detector energy, compensated by the use of state–of–the–art EAS simulation software.
Most experimental setups detecting UHECRs incorporate a large grid of surface detectors (SD array) measuring shower particles that arrive at ground level. The area occupied by this grid determines the flux of particles to be received according to the CR energy spectrum, while the separation between neighboring detector stations sets the primary particle high–energy limit we are still able to measure. From all the shower particles, only particles that hit our detectors in the array can actually be measured by this method, while information from the rest is lost. If we have a finer grid, we will obviously detect a larger number of shower particles and with it, a better resolution on the energy. Contrarily, if we have large gaps in the array, the obtainable primary particle energy can never be smaller than the energy resolution. Using a surface array also has an additional practicality in determining the arrival direction of the primary particle. This is nicely shown on figure 2.3, where a slanted shower is considered. Since every particle in the shower

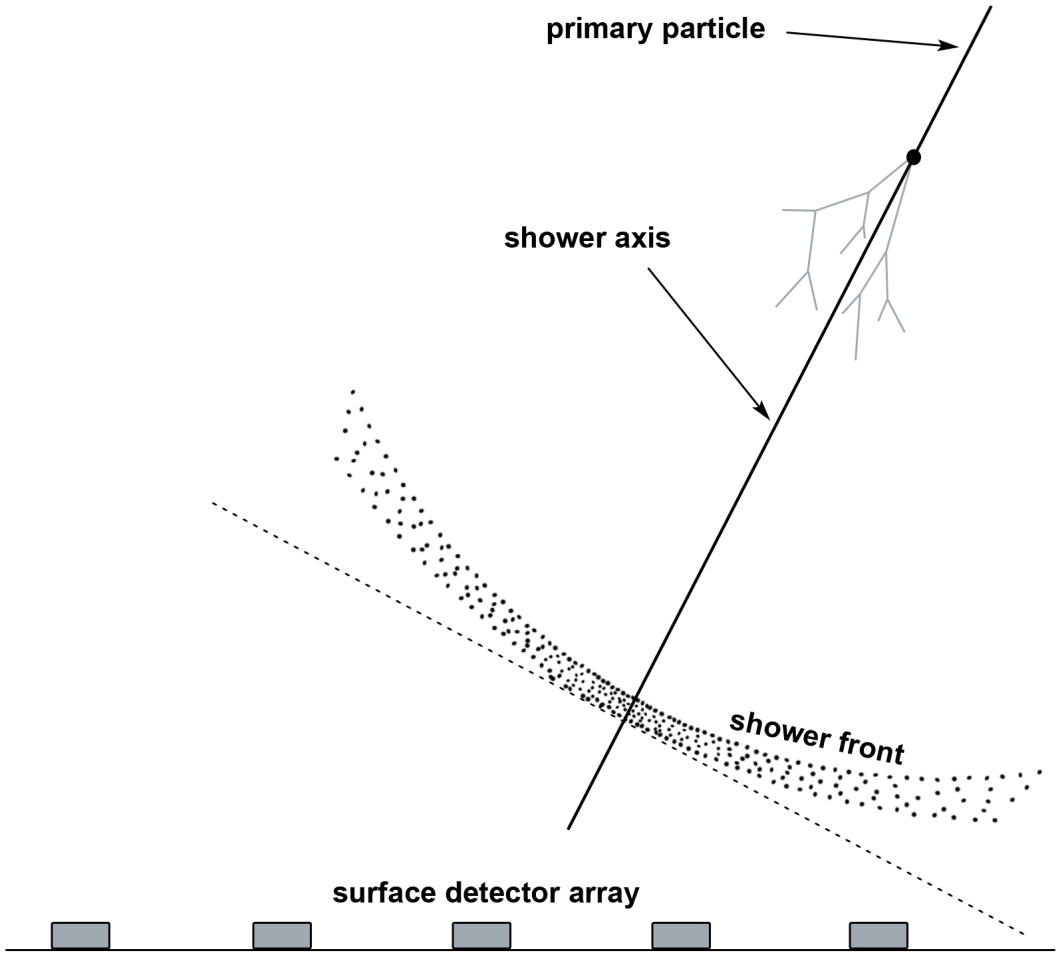

Figure 2.3: A representation of a slanted EAS and the geometry of the shower front as it nears the surface detector array (adapted from [3]).

traces its origin back to the primary interaction between the cosmic ray and an air molecule, the shower, as it travels deeper into the atmosphere, gains a slightly spherical shower front shape. This triggers neighboring surface stations with a

slight time delay, giving us the angle tilt of the shower axis. As a good example, the slanted shower on figure 2.3 will first produce a signal in the right–most detector, while the last one will be the left–most detector. Additionally, a detector closest to the shower axis will record the highest signal, as the number of particles close to the axis is much larger than farther away.
While surface detectors can not directly measure the longitudinal profile of an air shower, this becomes possible through a second detection method with the use of fluorescence detectors (FD). These detect UV light from collisions of secondary particles with nitrogen molecules in the air. Special FD detectors then focus the UV light with mirrors onto a grid of photomultipliers, thus tracking the development of an EAS. Naturally, a single FD detector will only be able to project a one–dimensional image of a shower to the photomultiplier grid, but including measurements from several differently positioned FD detectors, we are able to capture a single shower from multiple perspectives. With a better knowledge of the EAS path, the primary particle energy and arrival directions can be determined much more accurately. A flaw of the FD detection method is that a good signal to noise ratio can only be guaranteed during moonless nights with favorable atmospheric conditions. The result is a substantial reduction in duty cycle compared to surface detectors, from practically 100% down to around 10%.

3 Micro black holes

To fully understand the properties and structure of micro black holes (μBH), it is important to first introduce the concept of classical black holes in our 4–dimensional world. A formal definition of a black hole is actually fairly simple and loosely states that it is a massive object, a singularity in spacetime, with gravity so immense that nothing can escape it. Obviously, this definition is missing a vital piece of information concerning the range of this rule–breaking gravitational pull. A sort of invisible surface surrounding the black hole named the event horizon, limiting the region where escape velocity is larger than the speed of light c. The escape velocity of a particle or an object is the velocity it needs to achieve in order to escape the gravitational pull of another object of mass M, described as

$$E_{\text{kinetic}} = E_{\text{gravitational}} \quad \longrightarrow \quad v_{\text{escape}} = \sqrt{\frac{2GM}{r}}, \tag{3.1}$$

where $G = 6.67384 \times 10^{-11}\,\text{m}^3\text{kg}^{-1}\text{s}^{-2}$ is the gravitational constant and r is the separation between our escaping object and the center of the other massive object. For simplicity, we consider that mass M is compacted at a single point in its very center. Luckily, a black hole is a singularity in spacetime, thus this approximation fits well. Expressing the equation for r gives us the Schwarzschild radius of a black hole

$$r_s = \frac{2GM}{c^2} = M \cdot 1.485 \times 10^{-27}\,\text{m}\,\text{kg}^{-1}, \tag{3.2}$$

representing the radius of the event horizon. Note that equation (3.2) includes c instead of the escape velocity v_{escape}, since they are equal at the event horizon. To put it into perspective, the Schwarzschild radius for a black hole with mass comparable to the Sun ($M_\odot \approx 2 \times 10^{30}\,\text{kg}$) is equal to $r_s \approx 3\,\text{km}$. A good representation for the concept of a black hole and its event horizon is displayed on figure 3.1. On it, a particle is passing close to a massive object on the verge of becoming

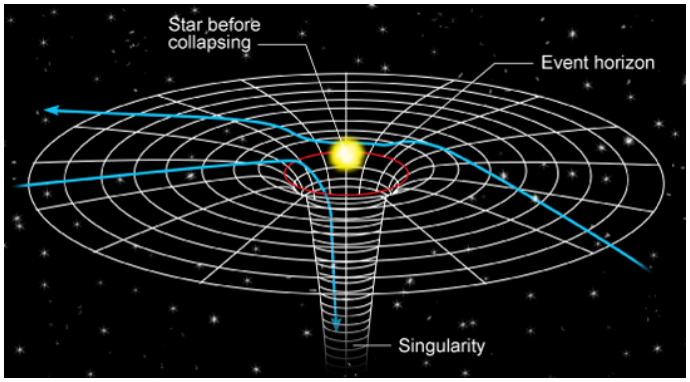

Figure 3.1: Particles moving on a geodesic (analogy of a straight line in curved 4–dimensional space) and their interaction with a star on the verge of becoming a black hole. One of the particles gets deflected, whereas the other crosses the event horizon and falls into a singularity (figure ref. [4]).

a black hole and deflects due to experiencing gravitational attraction or falls into the black hole when crossing the event horizon.
Interestingly enough, a black hole, according to the *no–hair theorem*, retains only three properties on the basis of which we classify it. These are mass, spin and charge. When a black hole has mass about 10–times the mass of the Sun it is classified as a stellar–mass black hole, while those with more than 5 orders of magnitude larger mass fall into the class of supermassive black holes, a class of objects that we could most likely find at the center of galaxies. The spin of a black hole determines its rotation speed and the charge gives information on the electrical charge it might carry. Through the last two properties, we give names to black holes, as presented in table 3.1. An initially charged black hole will highly

Table 3.1: Naming convention for black holes according to their spin and charge.

Charge (Q)	Spin/Rotation (J)	
	$J = 0$	$J \neq 0$
$Q = 0$	Schwarzschild BH	Kerr BH
$Q \neq 0$	Reissner–Nordström BH	Kerr–Newman BH

unlikely remain charged due to the large flux of incoming particles, whose charge could cancel the starting charge.
The actual formation of a classical black hole may follow the final stages of a dying star with a large enough mass. In its lifetime, a star will produce energy through fusion of elements. The excited particles in the star thus create thermal pressure and expand it, while gravity, acting in the opposite direction, tries to crush it. At the end of its lifetime, when fuel is running out, gravity starts overwhelming thermal pressure and the star begins collapsing with ever smaller radius and ever higher density of particles at its center. Although it might seem that at this point there is nothing else stopping the collapse into a black hole, it turns out that a fundamental principle of quantum mechanics is able to keep a star stable indefinitely. This is the famous Pauli exclusion principle, preventing fermions to occupy the same state, or in our case, the same position in space. Consequently, it creates a degeneracy pressure, further counteracting the gravitational collapse. It is therefore apparent that the only property able to determine, whether a star will form a black hole or not, is its mass. A black hole forms when the mass of the star is over or crosses the Chandrasekhar limit

$$M_{\mathrm{Ch}} = \frac{1}{m_p^2}\left(\frac{\hbar c}{G}\right)^{\frac{3}{2}} \sim 1.4 M_\odot, \tag{3.3}$$

where m_p is the proton mass, $M_\odot$ is the mass of the Sun and $\hbar$, c and G are reduced Planck, speed of light and gravitational constants, respectively. If, however, the mass is lower than M_{Ch}, neutron or electron degeneracy pressures stop the collapse and form neutrons stars or white dwarfs, depending on the pressure stopping the collapse.
Once a black hole is formed it continues acquiring additional mass from matter falling into its center, increasing its mass and the Schwarzschild radius, accordingly. Since most classical black holes that we observe in the Universe are rotating, the

falling matter creates an accretion disk, which emits X–rays due to constant friction between particles. However, these are not considered as emissions of the black hole. Once a particle crosses the event horizon, it can never escape. Nonetheless, it is predicted that black holes lose energy through two processes, Hawking radiation and gravitational waves. The former, as shown on figure 3.2, is pair production in the vicinity of the event horizon, where one particle crosses it and the other escapes. If this is a positron, an anti–particle with negative energy, it decreases black hole

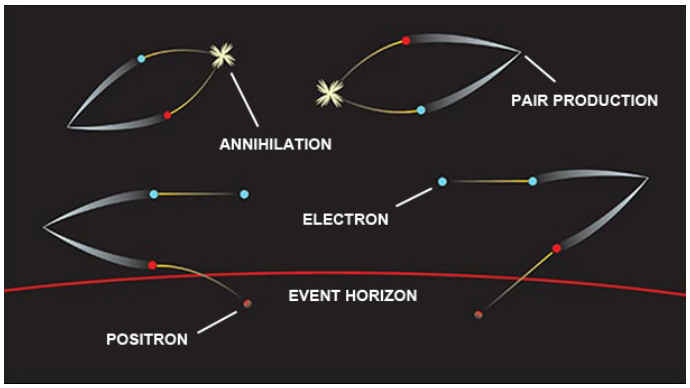

Figure 3.2: When pair production appears far from the black hole event horizon, the electron–positron pair can quickly annihilate. However, when this happens close to the event horizon, one can fall into a black hole and if it is a positron it reduces the black hole energy and make it seem as though the black hole emitted an electron (figure ref. [5]).

energy, seeming to the outside observer as an emission. Hawking temperature is calculated as

$$T_H = \frac{\hbar c^3}{8\pi G M k_B} \sim \frac{1.227 \times 10^{23}\,\mathrm{kg}}{M}\,\mathrm{K}, \tag{3.4}$$

where $\hbar$, c and G are constants already previously defined, while M is the black hole mass and $k_B = 1.3806 \times 10^{-23}\,\mathrm{J\,K^{-1}}$ is the Boltzmann constant. If we try to figure out how this compares to other known temperatures, the Hawking temperature for a solar mass black hole is $T_H \approx 10^{-7}\,\mathrm{K}$. Therefore, the cosmic microwave background (CMB) at its temperature 2.7 K is about 7 orders of magnitude higher.

3.1 Planck scale

In general, a semi–classical black hole can be formed with any mass, as long as it is above a certain limiting mass named the Planck mass $M_{pl} = 2.1765 \times 10^{-8}\,\mathrm{kg}$. Planck scale is defined as the energy scale at which all four fundamental forces are thought to be equal. In other words, when we are considering the Planck scale, we are thinking of the strength of the gravitational interaction that gets separated from the other three interactions at lower energies or the energy at which gravitational effects can not be neglected with respect to those of the other forces. Due to the equivalence between energy and mass, we can introduce a specific mass, names Planck mass, associated with the Planck scale

$$M_{\mathrm{pl}} = \sqrt{\frac{\hbar c}{G_N}}, \tag{3.5}$$

where G_N is just the normal gravitational constant G, but with an added index to separate it from a gravitational constant used in the following chapters. If we are to insert the constants in equation (3.5) and use natural units ($\hbar = c = 1$), Planck mass would take the value $M_{\text{pl}} = 1.2 \times 10^{19}\,\text{GeV}$, quite larger than that of the other three forces whose energy scales are below $10^3\,\text{GeV}$. Similarly, we can associate a characteristic length and characteristic time to different kind of interactions as shown on figure 3.3. Both of these characteristic quantities for the Planck scale

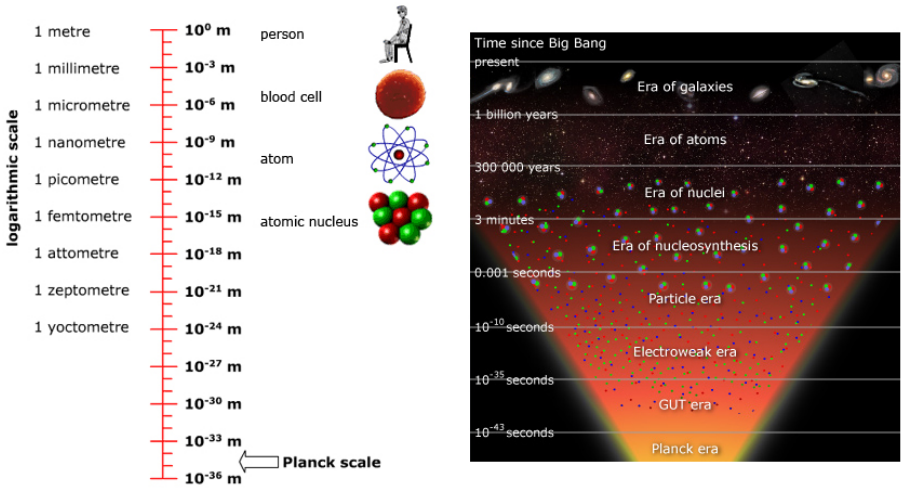

Figure 3.3: Characteristic representations of energy scales with different quantities. On the left, the Planck length is shown on a length scale (closest is the electroweak interaction at $\sim 10^{-18}\,\text{m}$) [6]. On the right, the evolution of the Universe follows eras, where forces are separated one by one and matter structures formed — i.e. hadrons, nuclei, atoms, molecules,... (figure ref. [7]).

are defined as

$$l_{\text{pl}} = \sqrt{\frac{\hbar G_N}{c^3}}, \qquad t_{\text{pl}} = \sqrt{\frac{\hbar G_N}{c^5}}, \tag{3.6}$$

making them extremely small ($l_{\text{pl}} \sim 10^{-35}\,\text{m}$, $t_{\text{pl}} \sim 10^{-44}\,\text{s}$). As seen on the right side of figure 3.3, depicting time since the Big Bang, each era denotes the separation of one fundamental force from the remaining forces. In the Grand Unification Theory era (GUT era) gravity has separated from the other three forces, in the electroweak era only electromagnetic and weak forces remain linked as the electroweak force and after that, thanks to the final electroweak symmetry breaking, the four forces finally exist separately. Further down the road, hadrons, nuclei, atoms and larger structures are formed. On the other hand, the length scale quite simply tells us about the typical resolution length below which we are to observe the force operating. The strong force, for example, has a characteristic length of $\sim 10^{-15}\,\text{m}$ and the combined electroweak force, the closest so far observed to the Planck scale, has it equal to $\sim 10^{-18}\,\text{m}$.

3.2 Hierarchy problem and extra dimensions

As it is fairly apparent from the previous chapter, the Planck scale, determining the strength of gravitational interactions, is far larger with respect to the typical

energy scales of any other interactions, leading to a hierarchy problem. If we are to compare the strength of gravitational interaction, characterized by the gravitational constant G_N, and the strength of electroweak interaction, originating from the Fermi constant G_F, we obtain a relative strength of interactions

$$\frac{G_N}{G_F} = \frac{G_N}{m_p^{-2} \cdot 10^{-5}} = \frac{6.7084 \times 10^{-39}\,\mathrm{GeV}^{-2}}{(0.938272\,\mathrm{GeV})^{-2} \cdot 10^{-5}} \sim 10^{-34}, \tag{3.7}$$

explaining that gravitation is 34 orders of magnitude weaker than the electroweak interaction. Since the strong interaction is only a few orders of magnitude stronger than the electroweak interaction, it is odd that gravity possesses such unique properties. It is feasible that this indeed is the case, but with the introduction of some exotic physics, we might be able to bring the strength of gravity closer to that of the electroweak force, while still explaining why we experience (measure) such a weak gravitational force. Before Albert Einstein introduced the theory of relativity, we viewed the world in three dimensions. After it, we found out that movement close to the speed of light unlocks a fourth dimension for such high–energy particles, behaving a bit differently than the three spatial dimensions. It is thus conceivable that increasing particle energy could permit it to traverse extra, previously unseen dimensions.

The additional dimensions that might exist according to this presumption can arise from a handful of extra dimension theories, but we will quickly present only the ADD model (Arkani–Hamed, Dimopoulos, Dvali) [8], as it was used for μBH simulations. With this model we introduce large extra dimensions, where the adjective *large* lets us know that the sizes of the dimensions will be much larger than the Planck length ($l_{\mathrm{pl}} \sim 10^{-35}\,\mathrm{m}$). However, what is more interesting is the fact that when crossing to a larger number of dimensions, which is, mathematically speaking, simple to do, we can observe the lowering of the quantum gravity energy scale M_*, set in our 4–dimensional world as the Planck mass. A gravitational potential between two arbitrary masses m_1 and m_2 will in a $(4+n)$–dimensional world behave as

$$V(r) \sim \frac{m_1 m_2}{M_*^{n+2} R^n} \frac{1}{r}, \tag{3.8}$$

where M_* is the quantum gravity scale, R the size of extra dimensions and r the separation between the two masses, assumed to be greater than R. Note that the behavior over r is exactly the same as what we experience in four dimensions and we can therefore create a connection between the quantum gravity energy scale in $(4+n)$ dimensions (M_*) and the same scale in 4 dimensions (M_{pl})

$$M_{\mathrm{pl}}^2 \sim M_*^{2+n} R^n. \tag{3.9}$$

Using this, we might observe physics corresponding to the quantum gravity energy scale in the TeV range, the energy achievable through present collider experiments. We must also take into account that requiring the quantum gravity scale to be this low gives some restrictions to the number of dimensions we can choose, the biggest indicator being the size of extra dimensions $R \sim 10^{30/n-19}\,\mathrm{m}$. Obviously, if we use one extra dimension ($n = 1$), their size would be so large ($R \sim 10^{13}\,\mathrm{m}$) that we would have observed it by now. However, choosing more dimensions gives the possibility of observing them at sizes of 1 mm or under.

At this point, a good question would be, what particles are actually able to traverse all $(4+n)$ dimensions. As we know from experimental results, all observed particles, which interact under the effect of three gauge forces (weak, strong and electromagnetic), including their mediators, behave as they should in a 4–dimensional theory, whereas gravitons are still proving to be extremely elusive. It is therefore reasonable to adopt a structure, where our 4–dimensional world resides on a so–called brane, while the extra n dimensions constitute the bulk. Standard model particles are localized on the brane, with three force carriers not losing any strength to the bulk. On the other hand, gravitons and possibly other exotic particles are able to traverse through the bulk, explaining why gravity has such small strength in our world. A simple way of imagining this is by looking at a perpendicular projection of a graviton on the brane, shown in figure 3.4. In 3 dimensions a perpendicu-

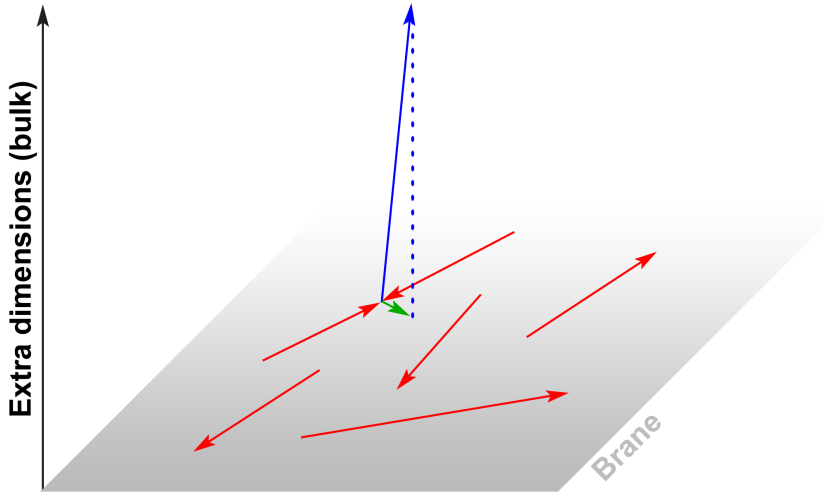

Figure 3.4: A simple representation of the brane–bulk structure of the ADD model. Standard model particles, contained in the brane are displayed with red vectors. A graviton, shown in blue, passes into the bulk, but still leaves a small component on the brane, shown in green, representing the weakness of gravity in 4 dimensions (adapted from [9]).

lar projection of a vector would produce its 2–dimensional representation. In the same way, we can imagine the strength of a graviton to be presented as a vector in $(4+n)$ dimensions and a perpendicular projection on the brane shows its strength in our 4–dimensional world.

3.3 Micro black hole production and evaporation

Physically speaking, it is completely possible to have a black hole of any size, since its Schwarzschild radius directly depends on the mass of the black hole in question, as presented with equation (3.2). Therefore, a micro black hole with mass around 1000 times larger than that of a proton ($m_p \sim 1\,\mathrm{GeV}$) would in a classical case have a radius close to the Planck length, where energy requirements to produce it would only be achievable at the time of the Big Bang or very shortly after. Any hope of discovering such μBHs would therefore be wishful thinking at most. However, with the help of the theory of extra dimensions, the production energy

reduces dramatically, possibly down to the TeV range. Depending on the type of μBH we are considering, the higher–dimensional spacetime metric was described by Tangherlini [10] for stationary and by Myers and Perry [11] for rotating μBHs. We will be skipping the metric, but a quick overview of both is included in [12], if needed. The Schwarzschild radius of a μBH in $(d+1)$ dimensions is defined as

$$r_s = \mu^{\frac{1}{d-2}} = \left(\frac{16\pi G_d M}{(d-1)\Omega_{d-1}} \right)^{\frac{1}{d-2}}, \tag{3.10}$$

where d is the number of all spatial dimensions (the normal 3 and extra n dimensions), G_d is the gravitation constant in d dimensions, M is the mass of the μBH and Ω_{d-1} is the area of a $(d-1)$–dimensional unit sphere. The higher–dimensional gravitational constant and the $(d-1)$–dimensional unit sphere are defined as

$$G_d = \frac{(2\pi)^{d-4}}{4M_*^{d-1}}, \qquad \Omega_{d-1} = \frac{2\pi^{\frac{d}{2}}}{\Gamma\left(\frac{d}{2}\right)}, \tag{3.11}$$

where M_* is the quantum gravity scale (the adjusted Planck scale in extra–dimensional theory) and $\Gamma(x)$ is the mathematical Gamma function. In the case of a non–rotating μBH, the Schwarzschild radius is the same as its horizon radius. The same can not be said for a rotating μBH where some of the energy is used up for the actual rotation, creating a smaller horizon radius

$$r_h = \frac{r_s}{\left[1 + \left(\frac{a}{r_h}\right)^2\right]^{\frac{1}{d-2}}}. \tag{3.12}$$

Here, a is a rotation parameter, displaying a measure of how fast a μBH is rotating and obtained by taking the angular momentum per unit mass. Clearly, when a micro black hole slows to a static case, the rotation parameter approaches zero, again equating the horizon radius and Schwarzschild radius.
Contrary to normal black holes, micro black holes are thought to form in high–energy particle collisions, where the two colliding particles have off–axis separation given by an impact parameter $b < 2r_h(d, M, J)$ and the collision center–of–mass energy is larger than the quantum gravity scale M_*. When these restrictions are met, a μBH is formed with an upper mass limit of the collision center–of–mass energy, a horizon radius r_h and angular momentum $J = \frac{bE_{\mathrm{CMS}}}{2}$. A representation of such a μBH forming collision is shown on figure 3.5. A further difference, compared to normal black holes, is their evolution. Since these are objects with an extremely small mass, compared to stellar mass black holes, they tend to lose energy through Hawking radiation and gravitational waves faster than they can gain by swallowing surrounding matter. Introducing Hawking temperature in $(d+1)$ dimensions definitely supports it

$$T_H = \frac{(n+1) + (n-1)a_*^2}{4\pi(1+a_*^2)r_h}, \tag{3.13}$$

where n is the number of extra dimensions $(n = d-3)$ and $a_* = \frac{a}{r_h}$ is the dimensionless rotation parameter. As an example, choosing $n = 2$ extra dimensions

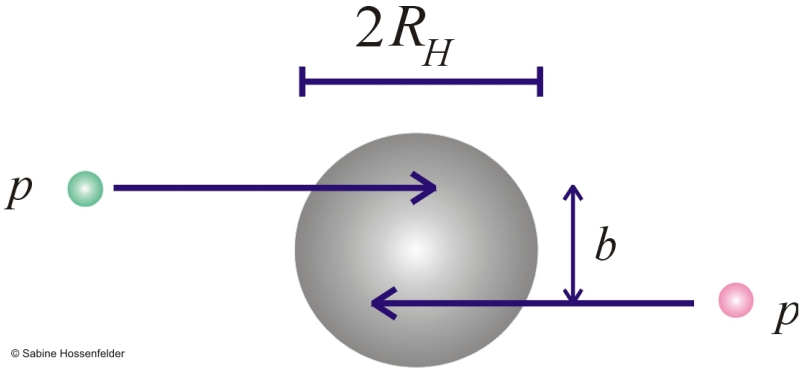

Figure 3.5: Two colliding particles with $E_{\text{CMS}} > M_*$ and an impact parameter $b < 2r_h(d, M, J)$ are able to form a μBH through the Hoop conjecture (figure ref. [13]).

$(d = 5)$, using equation (3.12) and limiting ourselves to a non–rotating μBH case $(a_* = a = 0)$, results to

$$T_H = \pi^{-1} \left(\frac{3}{4}\right)^{\frac{2}{3}} M_* \left(\frac{M_*}{M}\right)^{\frac{1}{3}} = 0.26276 \cdot M_* \left(\frac{M_*}{M}\right)^{\frac{1}{3}}. \tag{3.14}$$

If the quantum gravity scale M_* is of the order of $\sim 10^3$ GeV (this would solve the aforementioned hierarchy problem), with mass of the μBH not far above, making the fraction $\frac{M_*}{M} \approx 1$, equation (3.14) gives us a Hawking temperature on the order of $T_H \sim 10^2$ GeV. Converting this to a more human readable format using conversion factors found in appendix Appendix A, we learn that the smaller the μBH, the hotter it gets, in our case $T_H \sim 10^{15}$ K. The evolution of a μBH in time is represented on figure 3.6, depicting the four stages [12, 14]:

1. **Balding phase**
   A phase, where the μBH has a highly asymmetrical structure, with the asymmetries known as *hair*. During this phase, the μBH acquires a more symmetrical structure by emitting gravitation waves or other gauge fields, thus *loosing hair*.

2. **Spin–down phase**
   In this phase, the μBH, characterized by a slightly spheroidal shape due to non–zero impact parameter b, loses its energy and angular momentum through Hawking radiation. A faster rotating μBH will emit particles quicker.

3. **Schwarzschild phase**
   Now that the μBH is non–rotating, its shape is spherical and the principal energy loss is due to Hawking radiation. A μBH loses around 60% of its total mass in this and the previous phase.

4. **Planck phase**
   Having lost almost all of its energy, the mass of the μBH is now at the quantum gravity scale $(M \sim M_*)$. This, unfortunately, is the limit to where we can actually say something on its evolution, because without a valid quantum gravity theory, it can no longer be described semi–classically.

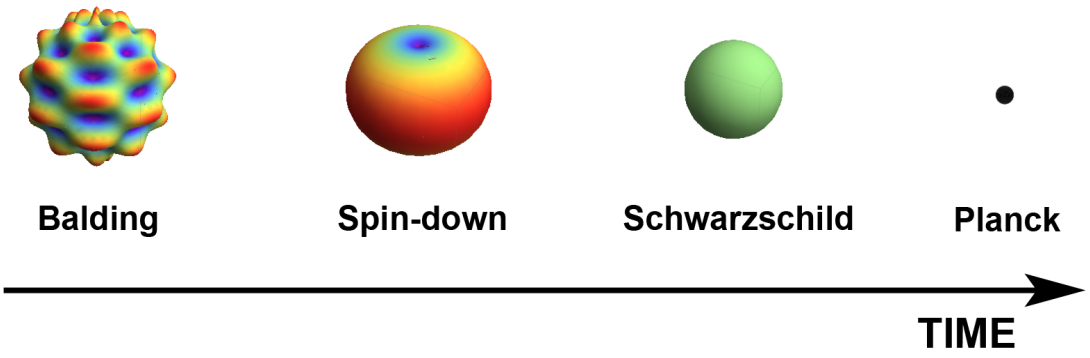

Figure 3.6: The four stages of μBH evolution, from the initially unstable balding phase to the mysterious Planck phase, where it crosses to the quantum gravity regime (adapted from [12]).

The middle two phases are dominated by Hawking radiation, that in black holes can be approximated with a black body radiation spectra. However, emission spectra for μBHs are modified by gravitational effects due to the curved geometry near the horizon. These are known as the grey–body emission spectra and are explained in the next chapter.

3.4 Experimental searches

As of yet, micro black holes and extra–dimensional theory both remain as purely theoretical concepts, lacking the experimental evidence to support them. The experimental searches performed at the Large Hadron Collider (LHC) in CERN currently by CMS and ATLAS collaborations so far did not single out any emission that might be ascribed to evaporating μBHs. Two plots on figure 3.7 clearly show the lack of particles that we would expect in a collision forming a μBH. The two plots differ because of the starting collision center–of–mass available energy $E_{\mathrm{CMS}} = \sqrt{s}$, left being the LHC run at 7 TeV, whereas the right was performed at 8 TeV after the collider upgrade. Data points that are observed in the experiment are shown as black dots with error bars, while the solid blue line and grey shading around it cover the background signal and the extent of the error on it, depending on the chosen fitting function. The horizontal axis displays the scalar sum of transverse energies E_T for a collection of jets, electron, photon and muon clusters that are rigorously selected depending on their transverse momentum p_T and pseudorapidity values and then counted together for events with a multiplicity of particles $N \geq 5$. The p_T cut is universally selected with a lower limit of 50 GeV for all types of particles, while pseudorapidity, a measure of the emission direction relative to the collision axis, was also limited separately for different particle types. Predictions from three different non–rotating μBH models with varying quantum gravity scale M_* (in the plots denoted as M_{D}) and number of extra dimensions n, are visible in these plots. These predictions were obtained by making simulations of the μBH stage with the BlackMax Monte Carlo event generator. No signature of μBHs is visible in these plots, where the experimental data falls in good agreement with the predicted Standard Model backgrounds even at large S_T. Even further comparison between current experimental results and simulations re-

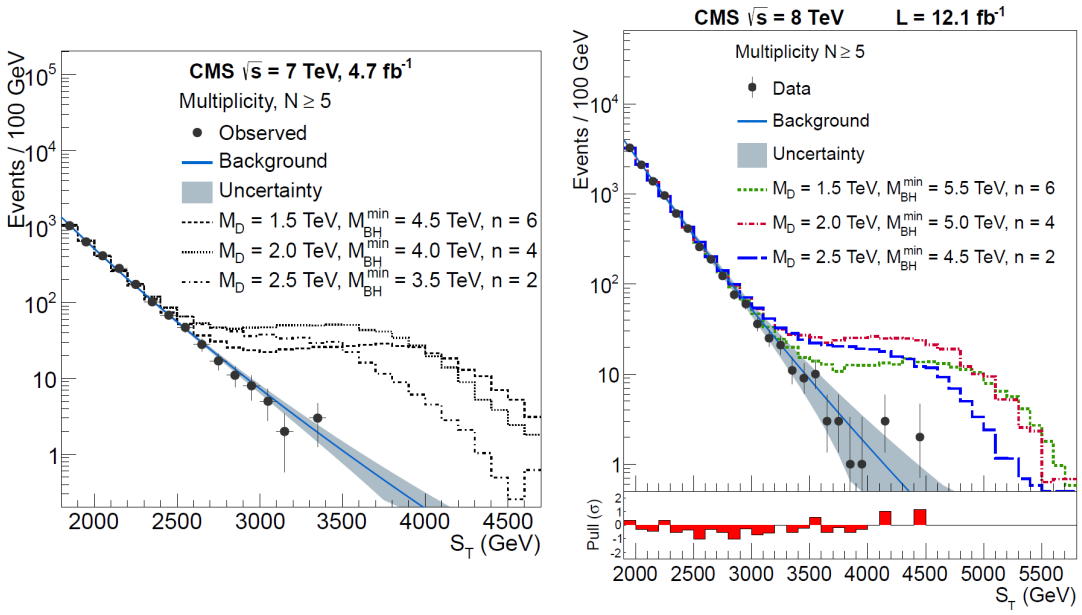

Figure 3.7: Results of experimental detection of μBH at the LHC (CMS detector) for runs at 7 TeV and 8 TeV collision energies. Black dots with error bars are data collected during the experiment, while the blue line with grey shaded area is the fit to the background signal. The three μBH models shown on each plot and simulated with BlackMax are clearly far from the observed values (figure ref. [15, 16]).

veals that the quantum gravity scale or the minimum black hole mass is larger then first predicted. The results obtained at 8 TeV rule out minimal μBH mass values of around 4.3 – 6.2 TeV. For any further or more indepth description of the experimental results, the reader is directed to the CMS [15, 16] and ATLAS result papers [17]. A highly anticipated upgrade to the LHC will enable it to run at 13 TeV and 14 TeV, thus increasing the chances of detecting μBHs or, in the worst case scenario, raising the minimum μBH mass limit and extra–dimensional quantum gravity scale even further.

4 Simulation of micro black holes in ultra–high–energy cosmic ray collisions

A collision of two particles might be able to produce a micro black hole that quickly decays into a collection of particles. For the purpose of describing the evolution, there are a few μBH event generators, each with their own level of detail. From the collection of possible event generators, CHARYBDIS [18] and BlackMax [19] are currently the most advanced, with the latter being able to simulate rotating micro black holes as well as non–rotating ones. Although a new version of CHARYBDIS [20] is available with rotating μBH generation, we used BlackMax for this thesis, because it received a later upgrade. The simulation process related to μBH creation and subsequent evaporation is described in section 4.1.
The resulting decay products are then gathered by hadronization software PYTHIA [21] or HERWIG [22] to produce parton and photon showers, include decays of short–lived particles and form hadrons from loose quarks. Any linking between BlackMax and PYTHIA is from now on designated as BlackMax/PYTHIA, whereas for the link to HERWIG it is BlackMax/HERWIG. The simulation description of the complete hadronization software process is presented in section 4.2.
Extensive air shower simulations are performed with CORSIKA [23], that needed to be checked for possible linking between BlackMax/PYTHIA and CORSIKA. Luckily, CORSIKA comes with a stack input option that simplifies the process, without a lot of code editing. The simulation part concerning extensive air shower (EAS) creation and development is described in section 4.3.
The complete simulation process schematically presented on figure 4.1 thus includes:

- **BlackMax:** Simulates the formation, evolution and evaporation of a μBH.
- **PYTHIA or HERWIG:** Simulates parton showers, proton showers, particle decays and hadronization, creating a large number of stable particles and hadrons in the process.
- **CORSIKA:** Simulates EAS creation and development, with the use of its stack input option, that permits us to use stable particles from previous steps as secondary shower particles instead of primaries.

Although we did not use a direct link between BlackMax/PYTHIA and CORSIKA (programs run separately), the latter still dictates initial collisions between proton and molecules in the atmosphere. The reason for this is that we can run BlackMax at a predetermined energy and then use exactly the same energy when performing an EAS simulation. The only thing that needs to be done with the list of all stable particles, before giving it to stack input, is to transform energies and momenta to the laboratory frame. This and the correction to the first interaction calculation is presented in the last section of this chapter.

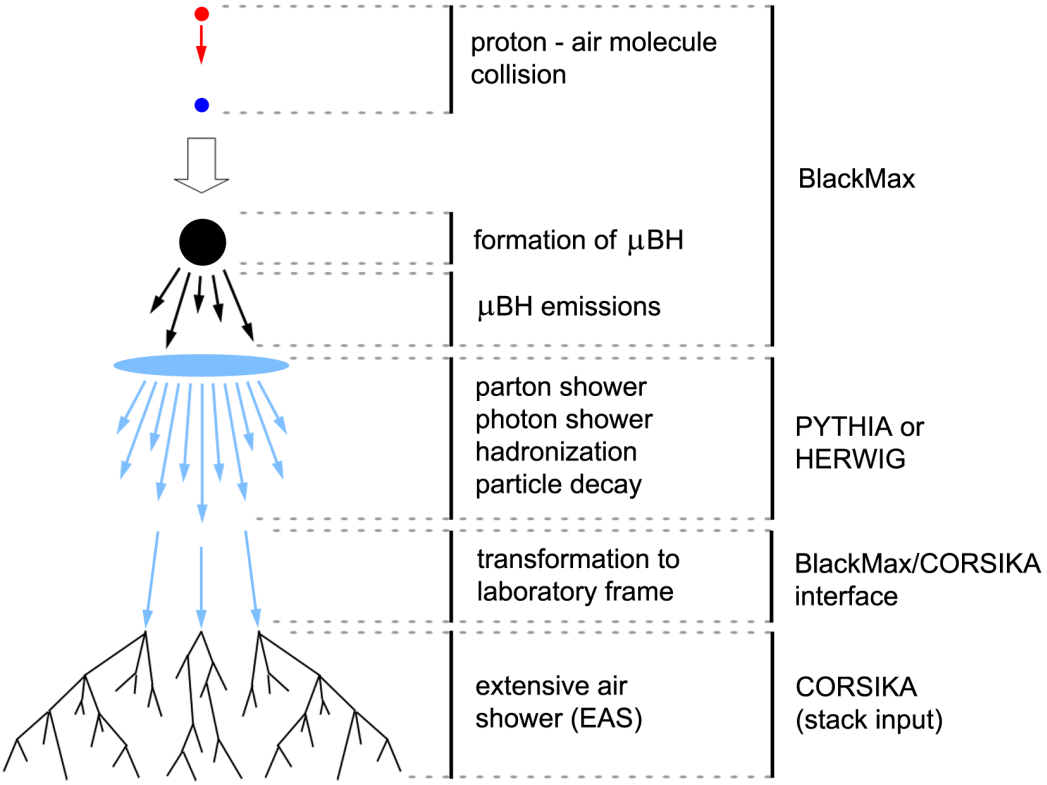

Figure 4.1: A schematic representation of the complete process of simulation. Only BlackMax and the hadronization software (PYTHIA or HERWIG) are actually linked, while CORSIKA is run separately by only using the list of particles surviving hadronization.

4.1 Micro black hole creation and evaporation

BlackMax is a μBH event generator, with two initial colliding particles that form a micro black hole, with the use of four possible scenarios.

- **A non–rotating μBH on a tensionless brane**
  The simplest case, where a formed μBH is non–rotating and follows the large extra dimension theory (ADD model), with only gravitons being able to traverse across the bulk.

- **A non–rotating μBH with a non–zero tension parameter**
  The tension parameter incorporates a modified bulk structure that affects its emission spectra. For now, BlackMax can only handle the situation with two extra spatial dimensions ($d = 5$).

- **A non–rotating μBH with fermion brane spitting**
  The split–fermion model has multiple branes, where fermions can propagate, while gauge bosons and gravitons are able to traverse across the bulk.

- **A rotating μBH on a tensionless brane**
  The only case, where BlackMax takes into account an initial non–zero angular momentum of the μBH. Current limitations only permit particles to live on the brane thus completely suppressing graviton emisson.

Accompanying each scenario are other free parameters that affect the course of simulation, from initial particle information, number of simulations, extra dimension properties, parton distribution functions and μBH mass limits to more advanced parameters, such as loss factors and suppression factors. Keeping in mind that μBHs are still purely theoretical, these free parameters give us the possibility to tailor μBH generation to our specific field of research.
Since the program was originally created for the intended use with colliders, the possible initial collisions are between two protons, a proton and an antiproton and between an electron and positron. The last possibility can be used for predictions of μBH generation at electron–positron colliders, while the first two are for the Large Hadron Collider (LHC). However, initial center–of–mass energy of the collision E_{CMS} is actually not limited, therefore BlackMax is also applicable at higher energy processes, like collisions of cosmic rays with atmospheric nuclei. The only limiting cases for a μBH formation come from our definition of the quantum gravity scale M_*, minimum mass M_{min} and maximum mass M_{max} of the μBH. At the quantum gravity scale a μBH already crosses to the Planck phase, after which it can not be simulated without a valid quantum gravity model. This in turn sets the relation $M_* < M_{\mathrm{min}} < E_{\mathrm{CMS}}$, where M_{min} should be large enough to avoid any irregularities due to quantum effects. The maximum mass can be set to a higher value than the center–of–mass energy, but there is no point in doing so, as this is not possible from obvious energy conservation reasons. For any simulations presented in this work, we adopted the simplification $M_{\mathrm{max}} = E_{\mathrm{CMS}}$. A direct effect on the μBH mass comes from the mass–loss factor f_{E}, determining the amount of mass it will lose before fully forming. Similarly, the momentum–loss f_{P} and angular momentum–loss factors f_{L} will reduce the respective values of momentum and angular momentum of a μBH. The loss of mass, momentum and angular momentum happens in the balding phase, a process approximately described by BlackMax with an emission of a couple of particles, either gravitons or photons, leaving values

$$\begin{aligned} E &= E_{\mathrm{in}} f_{\mathrm{E}}, \\ P_{\mathrm{z}} &= P_{\mathrm{z\,in}} f_{\mathrm{P}}, \\ J' &= L_{\mathrm{in}} f_{\mathrm{L}}, \end{aligned} \tag{4.1}$$

where E, P and J' are energy, momentum and angular momentum after losses and index "in" denotes their initial values.
Possible parameters for setting extra dimension properties are the number of extra spatial dimensions $n = d - 3$, size of the brane and extra–dimension size. When taking into account scenarios with a split–fermion model and non–zero tension, we can also set parameters for these. Suppression factors will give a suppression on emissions, because these will inherently try to reduce the μBH charge, color and angular momentum, not increase them. BlackMax comes with a collection of parton distribution functions (PDF) that we use for μBH formation and cross–section calculation. However, with the use of the LHAPDF library [24] of PDFs, we can choose between a much larger and updated collection, where those supplied with BlackMax are numbered from 10000 to 10040 (*cteq6*). In a recent update of BlackMax, a possibility for string–balls has also been included, but this is beyond the scope of this thesis and we have not been using it.

4.1.1 Physics background of BlackMax

After importing user–given input parameters, BlackMax will calculate the impact parameter b of a two particle collision, selected as a random fraction of the maximal impact parameter

$$b_{\max} = 2r_h^{(d)} = 2 \cdot \frac{k(d)}{M_* \left[1 + \left(\frac{d-1}{2}\right)^2\right]^{\frac{1}{d-2}}} \left(\frac{E_{\mathrm{CMS}}}{M_*}\right)^{\frac{1}{d-2}} \left[\frac{1 - f_{\mathrm{E}}}{E_{\mathrm{CMS}}(A_0 + A_1 \cdot R)}\right]^{\frac{1}{d-2}}, \tag{4.2}$$

where f_{E} is the mass–loss factor, R is a pseudo–random number on the interval $[0.0, 1.0)$ and d is the number of all spatial dimensions (3 normal and the added extra dimensions n). A_0, A_1 and $k(d)$ are defined as

$$\begin{aligned} A_0 &= \frac{1 - f_{\mathrm{E}}}{M_{\min}}, \\ A_1 &= \begin{cases} \frac{1}{E_{\mathrm{CMS}}} - A_0, & \frac{1-f_{\mathrm{E}}}{M_{\max}} < \frac{1}{E_{\mathrm{CMS}}} \\ \frac{1-f_{\mathrm{E}}}{M_{\max}} - A_0, & \frac{1-f_{\mathrm{E}}}{M_{\max}} \geq \frac{1}{E_{\mathrm{CMS}}} \end{cases}, \\ k(d) &= \left[2^{d-3} \cdot \pi^{\frac{d-6}{2}} \cdot \frac{\Gamma\left(\frac{d}{2}\right)}{d-1}\right]^{\frac{1}{d-2}} \end{aligned} \tag{4.3}$$

to somewhat simplify the starting equation. $\Gamma(x)$ is the mathematical Gamma function.

Cross–section of the collision is calculated directly from (4.2) with the addition of parton distribution functions, before even starting the μBH formation process. Therefore, no matter how many events we choose to generate, BlackMax will still repeat this calculation 10^5 times to statistically choose the best possible value for the cross–section. Figure 4.2 shows the dependence of cross–section on the number of extra dimensions and the center–of–mass energy of the collision. As an example,

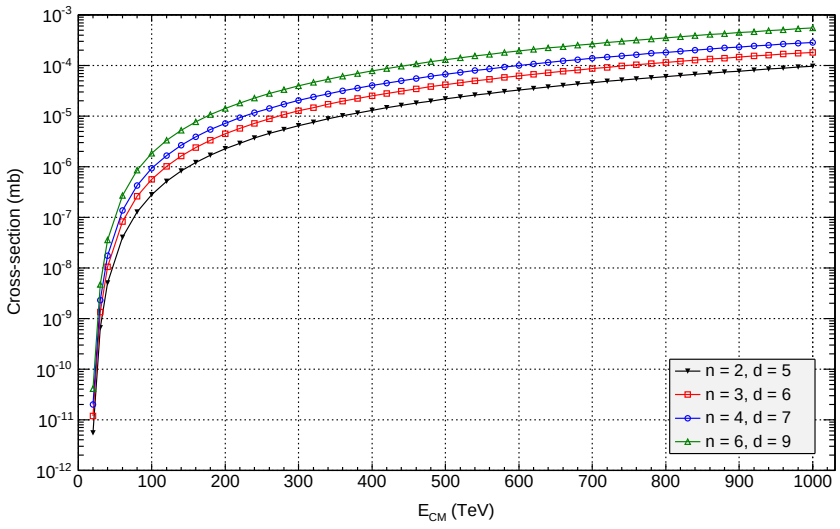

Figure 4.2: Cross–section of a two proton collision in the formation of a μBH for a range of extra dimensions $n = d - 3$ and center–of–mass energies E_{CMS} between 20 TeV and 1000 TeV. The quantum gravity scale was set to $M_* = 5$ TeV.

the cross–section of a collision between a CR proton and atmospheric atoms is on the order of 100 mb [25]. When the cross–section is calculated, we come to the actual μBH formation process, where a μBH is created when

$$u > \left(\frac{M_{\min}}{E'_{\mathrm{CMS}}}\right)^2 > \left(\frac{M_{\min}}{E_{\mathrm{CMS}}}\right)^2, \tag{4.4}$$

where u is the parton fraction of one of the colliding partons and $E'_{\mathrm{CMS}} = \sqrt{s'} = \sqrt{us} = E_{\mathrm{CMS}}\sqrt{u}$ is the actual center–of–mass energy of the two colliding partons. The created μBH losses part of its energy through shedding *hair*, either by emitting two gravitons or two photons in case graviton emission is suppressed. These initial photon emissions implemented in BlackMax are not physical and serve only to reduce the energy of the μBH according to the selected mass–loss factor. Needless to say, they have to be omitted from the output for any further simulations to eliminate any unwanted artifacts. Continuing on, BlackMax enters the energy and angular momentum loss phase through Hawking radiation supplied by the grey–body emission spectra, describing both spin–down and Schwarzschild phases. The spectra are read from accompanying spectra files, calculated for fermion, vector gauge boson, scalar and graviton fields. For the rotating scenario, they include a range of dimensionless rotation parameters

$$a_* = \frac{a}{r_h} = \frac{J}{M_{\mathrm{BH}}}\frac{n+2}{2r_h} = [0.0, 1.5], \tag{4.5}$$

and angular momentum quantum numbers $m_l = [-9, 9]$ to account for rotation speed reduction due to emission of particles. In equation (4.5), $J = \sqrt{j(j+1)}\hbar$ is the angular momentum, a the rotation parameter and M_{BH} the current μBH mass. Grey–body emission spectra then follow a power spectrum

$$r_h\frac{\mathrm{d}^2E}{\mathrm{d}t\,\mathrm{d}\omega} = \frac{1}{2\pi}\sum_{l,m_l}|A_{l,m_l}|^2\,\frac{r_h\omega}{\mathrm{e}^{(r_h\omega - m r_h\Omega)/(r_h T_H)} \mp 1} \tag{4.6}$$

where A_{l,m_l} is the grey–body factor, ω energy of the emitted particle and T_H (Hawking temperature) and Ω (rotation velocity) are defined as

$$\begin{aligned} T_H &= \frac{(n+1) + (n-1)a_*^2}{4\pi(1+a_*^2)r_h}, \\ \Omega &= \frac{a_*}{(1+a_*^2)r_h}. \end{aligned} \tag{4.7}$$

An example of a grey–body emission spectrum is displayed on figure 4.3 taken directly from a run of the BlackMax program. It stands to reason that all above equations have $a_* = 0$ for a non–rotating μBH, leaving a simple spectrum without oscillations. At this point, any suppression factors that we have set are taken into account and suppress some of the emissions or favor only emissions that reduce the charge and color of the μBH. According to the BlackMax manual, we have set suppression factors to the recommended values of 0.2. At the very final stage of the simulation, a graviton is emitted following a final burst scenario as a plausible outcome of the Planck phase thus conserving energy, momentum and quantum numbers of the μBH. More on BlackMax, its input parameters and program structure can be found in [19] or [26].

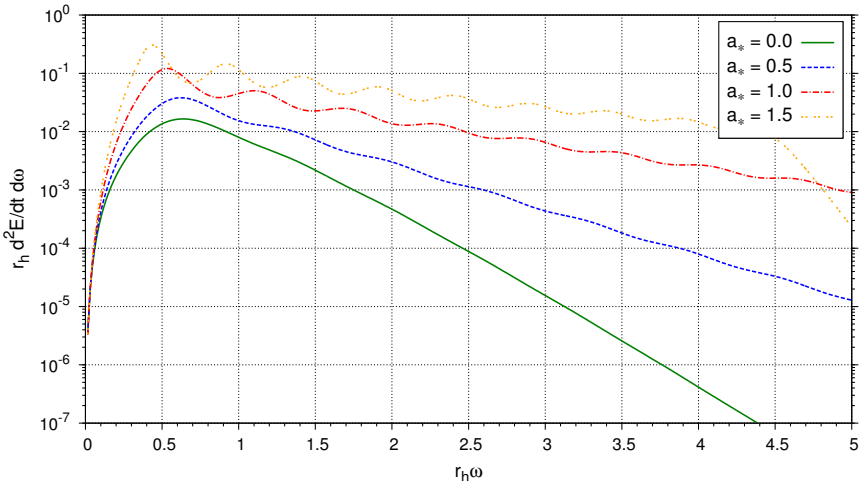

Figure 4.3: Grey–body emission spectra for four different values of a dimensionless rotation parameter a_*. A rotating μBH ($a_* > 0$) will have oscillations on the spectrum that gradually decrease as the μBH slows towards a non–rotating case ($a_* = 0.0$).

4.1.2 Micro black hole decay products

In general, BlackMax will produce an output of initial collision partons, emitted particles and track the position (recoil) of the μBH. It supplies the user with color, charge, energy and momentum for each emitted particle. As an example, figure 4.4 shows the amount of particles and antiparticles per μBH event (a complete treatment of one μBH is considered as one event), arranged into groups after μBH evaporation for two center–of–mass energies (14 TeV and 100 TeV). The larger

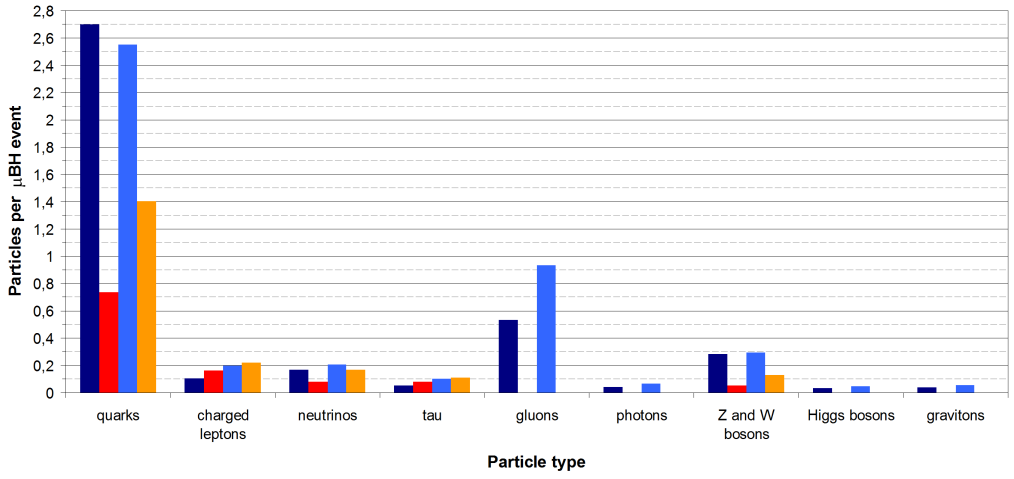

Figure 4.4: An arrangement of particles (dark–light blue) and antiparticles (red–orange) into groups, with y–axis displaying particle count per μBH event. The first two columns of each group are for a simulation with $E_{\mathrm{CMS}} = 14\,\mathrm{TeV}$ and the second two columns for $E_{\mathrm{CMS}} = 100\,\mathrm{TeV}$. $n = 2$ extra dimensions were used and 10^5 μBH events generated.

number of particles for the $E_{\mathrm{CMS}} = 100\,\mathrm{TeV}$ case can easily be explained by the fact that the larger the mass of the μBH, the more emissions it produces before

getting to the Planck phase. On the other hand, the different contributions from particles and antiparticles, especially visible with quarks, comes from our choice of initial collision particles. Specifically, when colliding two protons, the partons interacting can only be quarks or gluons, but if we would have used a proton–antiproton collision, we would have antiquarks to our disposal as well.
To simplify any simulations to be done after the evaporation, BlackMax outputs initial partons and emitted particles into a standardized Les Houches Accord (LHA) type format [27], used in a number of other Monte Carlo simulators. We used a similar feature for a histograming function that immediately produces histogram plots, without creating any extra time– and resource–consuming particle listings. This is particularly useful at extremely high energies and simulations following the evaporation due to a large number of output particles. The LHA event format stores information about the particles inside a HEPEUP common–block for every particle produced. This information is stored at the end of each generated event and can be used for user created applications. A histograming function then simply checks the binning arrangement and registers a count at the bin range for each particular particle. Histograms with a logarithmic x–axis range (energy E, transverse momentum p_T) were considered beforehand and their bin widths set up in a way to remain constant on a logarithmic scale. Additionally, we distributed all emitted particles by their type into seven groups:

- **Quarks:**
  As the constituents of mesons and baryons, they are an important group for comparison to further hadronization simulations. Apart from their role in hadron creation, the can also emit gluons through parton showers.

- **Gluons:**
  Their main role is in parton showers, because they can give rise to gluon or fermion emissions. Through this process, we arrive from a handful of particles at μBH evaporation to a large parton shower.

- **Charged leptons:**
  At high energies, their main energy loss process is through bremsstrahlung radiation, producing low energy photons.

- **Neutrinos:**
  As stable particles, neutrinos are good indicators for weak interactions in the processes following μBH evaporation.

- **Photons:**
  Similar to neutrinos, but as indicators for electro–magnetic interactions, bremsstrahlung radiation, annihilation or other decay processes that produce them.

- **Z^0 and $W^{\pm}$ bosons:**
  Another type of indicators for weak interactions, but due to their decay rate, they will not survive for long, making them useless for any pre– and post–hadronization comparisons.

- **Tau leptons:**
  They are treated separately, because of their complex dynamics with several decay modes. Thanks to that, tau leptons will not survive the hadronization process.

For example, figure 4.5 holds five histograms that give us some information about the distribution of the above–mentioned groups immediately after μBH evaporation stage. Rapidity φ and pseudorapidity η are measures of the direction of particle emissions relative to the collision axis. They are defined as

$$\varphi = \frac{1}{2}\ln\left(\frac{E+p_Z}{E-p_Z}\right), \qquad \eta = \frac{1}{2}\ln\left(\frac{|\mathbf{p}|+p_Z}{|\mathbf{p}|-p_Z}\right), \tag{4.8}$$

where E is particle total energy ($E^2 = \mathbf{p}^2 + m^2$), $\mathbf{p} = (p_X, p_Y, p_Z)$ is particle total momentum and p_Z is the momentum along the collision axis (also known as longitudinal or forward momentum). Rapidity and pseudorapidity differ only when considering massive particles, for which rapidity is much more appropriate. A quick glance at their histograms uncovers that emitted particles are mostly directed perpendicular to the initial collision direction ($\eta \simeq 0 \;\rightarrow\; \theta \simeq 90°$). The

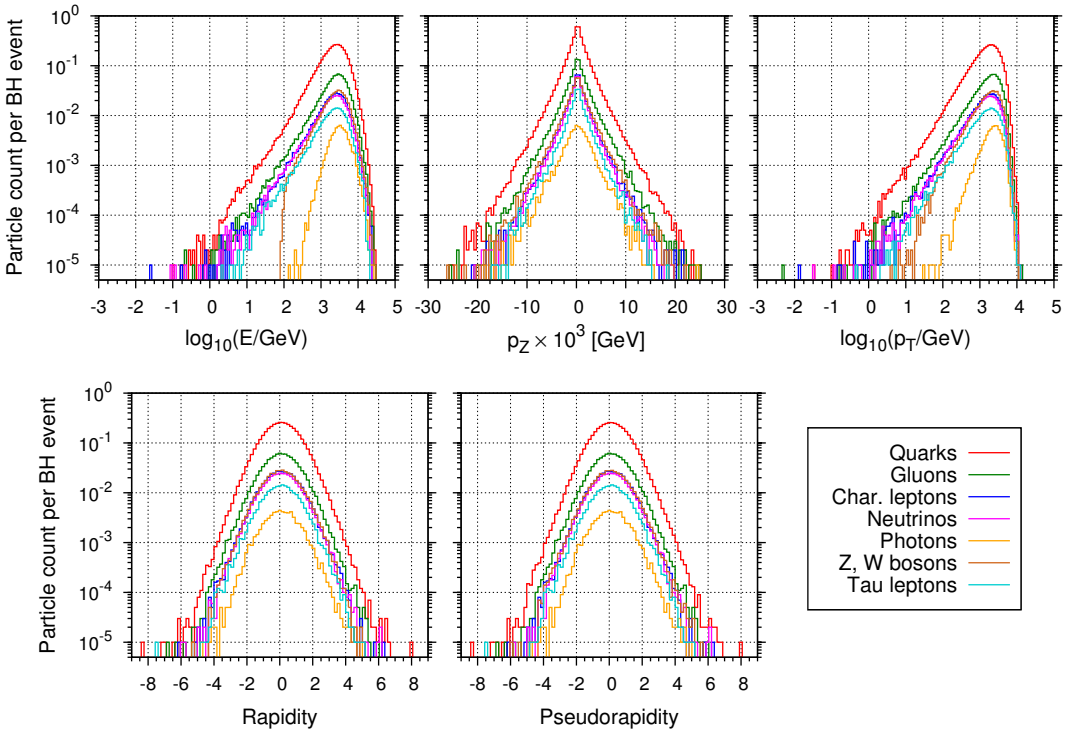

Figure 4.5: Histograms for energy E, forward momentum p_Z, traverse momentum p_T, rapidity and pseudorapidity for particles following μBH evaporation, simulated by BlackMax. Center–of–mass energy of initial collision was set to $E_{\mathrm{CMS}} = 100\,\mathrm{TeV}$, with $n = 2$ extra dimensions and 10^5 μBH generated events.

output from BlackMax, including separate partons, is not used directly as an input for CORSIKA and must therefore first pass through an additional parton shower and hadronization simulation software. PYTHIA and HERWIG are generally used for just such purposes.

4.2 Hadronization of micro black hole decay products

Hadronization is the formation of hadrons from gluons and quarks, because these do not exist as free particles. The software for it, however, contains extra steps to get to the actual hadronization part, namely parton and photon showers. These consist of further fermion and gluon emissions, ordered according to decreasing transverse momentum, arising from gluons and photons according to renormalization theory. Lastly, hadronization software assembles quarks and gluons into hadrons. Additionally it provides decays of any short–lived particles and produces a final collection of stable particles. The current version of BlackMax already comes with a possible interface to PYTHIA and with instructions given in the manual, it is fairly easy to setup. The interface checks for particles emitted from a μBH and through an external function supplied with BlackMax (*initpy.f*), initializes the hadronization procedure. At this stage, it is possible to define new values to masses, decay widths or other particle process parameters that the process will adopt in order to equate them to BlackMax. Recently, a new C++ structure based PYTHIA (version 8.x) had been developed, but for the purpose of this thesis, we have been using version 6.4.28, because BlackMax currently does not provide an interface with newer versions. Table 4.1 holds the masses and decay widths we changed in PYTHIA according to the latest PDG [28] measurements. At a first

Table 4.1: Masses and decay widths for particles in PYTHIA and HERWIG, with the values we used to equate them (u, d, c, s and b quarks) and include latest measurements from PDG [28]. Decay widths Γ for quarks other than the top quark are set to zero, since they are considered to be stable in both programs.

Particles	PYTHIA		HERWIG		Used values	
	m [GeV]	Γ [GeV]	m [GeV]	Γ [GeV]	m [GeV]	Γ [GeV]
u, d	0.33	0	0.32	0	0.33	0
s	0.5	0	0.5	0	0.5	0
c	1.5	0	1.55	0	1.5	0
b	4.8	0	4.95	0	4.8	0
t	175	1.39816	174.3	1.64553	173.5	1.99
H	115	0.00367	115	0.0037	115.5	inherent
Z^0	91.188	2.47813	91.188	2.495	91.1876	2.4952
$W^{\pm}$	80.45	2.07115	80.42	2.12	80.385	2.085

glance, the quark masses in table 4.1 are not correct, but one needs to remember that these are running masses, depending on the experiment energy. The decay width of Higgs bosons is hard to change inside HERWIG and since the values in both hadronization softwares are fairly similar, we left them as they are. Linking a high–energetic run of BlackMax to PYTHIA calls for further editing, due to the large amount of particles produced by the hadronization process. The original version of PYTHIA, for example, only has space for 4000 particles per event and that is more than enough for lower collider energies. For a successful run at

cosmic–ray energies, however, we had to increase this number to 10^4 (the highest recommended value).
On the other side, setting up HERWIG was a bit of a challenge, but after a few tries it was apparent that some of the interface codes had to be minutely changed. The HERWIG version we used for this thesis was version 6.520. In *GetPdf.f* code, supplied with BlackMax, a default parameter had to be changed to `parm(1)='HWLHAPDF'`. At the same time, this value had to be supplied inside the HWIGUP subroutine to the `PDFNUC` variable. Together, these ensure that the correct PDFs are used for simulations and we do not run into any errors at the very beginning. The initialization call had to be replaced with `HWUINC` in the interface code *initpy.f* to interface with the correct hadronization software. Equally, the hadronization function in the BlackMax code needed to be changed to a collection of functions, because HERWIG handles each stage of the hadronization separately. Another change had to be made to the way HERWIG reads particle codes. These are different than the PDG set Monte Carlo particle numbering scheme, creating some difficulties when reading initial particle types. Luckily, it already comes with a translator between PDG particle code, internal identity code and particle name. After these changes, available particle spaces had to be increased to 10^4, just like in PYTHIA, while masses and decay widths were edited according to table 4.1.
Setting up both hadronization softwares, we performed comparative simulations for BlackMax/PYTHIA and BlackMax/HERWIG interfaces and then used the same histograming functions as for the normal BlackMax particle output. Since some of the particle groups are no longer present — i.e. quarks and gluons were transformed into baryons and mesons, while charged bosons and tau leptons decayed — the initial seven groups are reduced to only five (baryons, mesons, charged leptons, neutrinos and photons), but the reasoning for the grouping is still the same. The histograms are displayed on figure 4.6 for particles after PYTHIA treatment and figure 4.7 for the treatment with HERWIG. The input parameters used for both simulations were the same as for the case on figure 4.5, with the more important ones being:

- Non–rotating μBH scenario with 2 extra non–split dimensions ($n = 2$).
- 100000 generated μBH events, with starting proton–proton collision at energy $E_{\mathrm{CMS}} = 100\,\mathrm{TeV}$.
- M_* chosen to be 5 TeV and minimum μBH mass twice as large $M_{\mathrm{min}} = 10\,\mathrm{TeV}$.
- Selected parton distribution function is *cteq6ll*, LHAPDF number 10042.
- Mass, momentum and angular momentum loss factors all set to 0.15.
- Graviton emission is turned on.

All plots are normalized to a single μBH event to permit direct comparison to histograms just after μBH evaporation (figure 4.5), though some of the ranges on the axes have been changed for clarity. Looking at all three rapidity or pseudo-rapidity histograms, we clearly see that only neutrinos have more or less retained their shape, with extra neutrinos coming from weak decays (for instance from $\mathrm{W}^{\pm}$ and Z^0 bosons). The rest of the particle types have taken a completely different shape and now additionally have high–rapidity parts, coming soft and collinear emissions generated in parton showers. In other words, there are now more par-

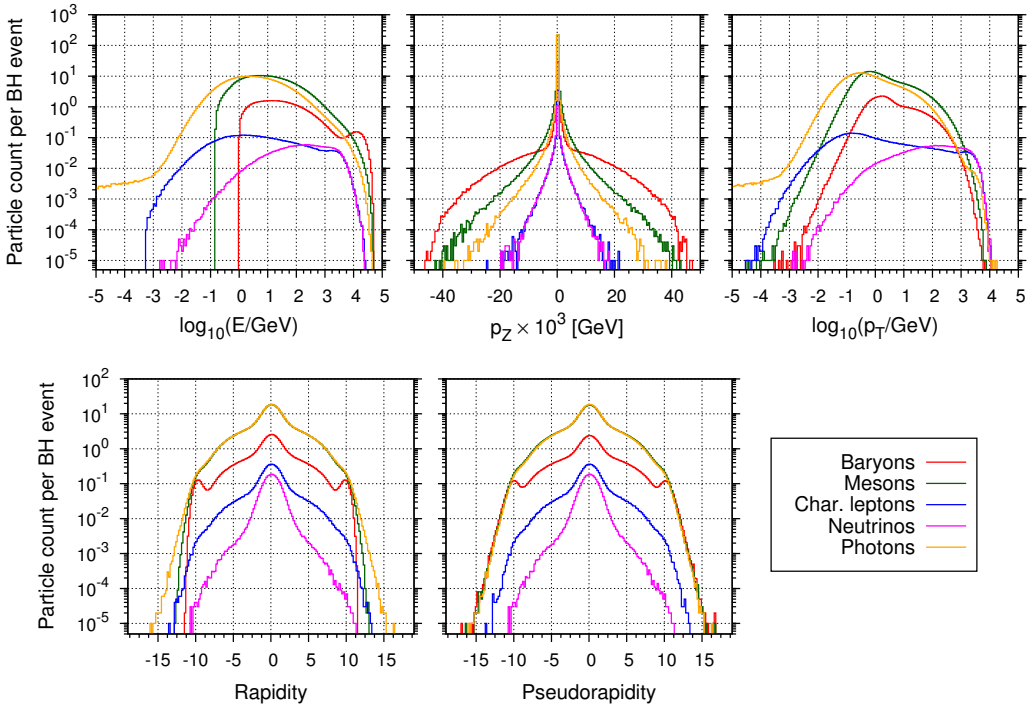

Figure 4.6: Histograms for energy E, forward momentum p_Z, traverse momentum p_T, rapidity and pseudorapidity for particles following the BlackMax/PYTHIA interface simulation. Center–of–mass energy of initial collision was set to $E_{\mathrm{CMS}} = 100\,\mathrm{TeV}$, with $n = 2$ extra dimensions and 10^5 μBH generated events.

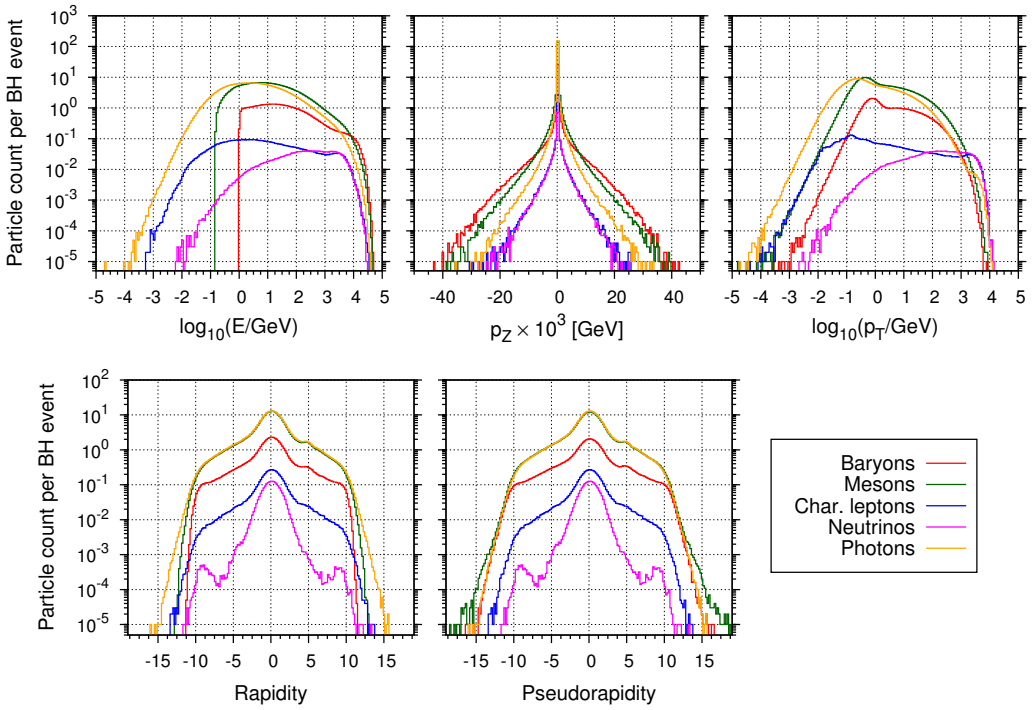

Figure 4.7: Histograms for energy E, forward momentum p_Z, traverse momentum p_T, rapidity and pseudorapidity for particles following the BlackMax/HERWIG interface simulation. Center–of–mass energy of initial collision was set to $E_{\mathrm{CMS}} = 100\,\mathrm{TeV}$, with $n = 2$ extra dimensions and 10^5 μBH generated events.

ticles directed in the forward (backwards) direction with large positive (negative) p_Z momentum values. The sudden drops in baryon and meson energy histograms is a direct consequence of relativistic energy

$$E^2 = m^2 + \mathbf{p}^2, \tag{4.9}$$

where the minimum energy turns out to be the rest mass of a particle. The limiting energy for mesons is dictated by pions with mass around $m_{\text{meson}} \simeq 140\,\text{MeV}$, while that of baryons is $m_{\text{baryon}} \simeq 1\,\text{TeV}$.
Photon histograms might be a bit hard to understand at first and common sense would tell us that they should be more like neutrinos due to their neutrality. Hadronization of μBH events forms a large number of π^0 mesons, with their most probable decay channel ($P \simeq 98.8\%$) into two photons ($\pi^0 \longrightarrow \gamma\gamma$). This leaves a remarkable similarity between histograms for photons and mesons. The comparison can clearly be seen on figure 4.8 displaying the rapidity for a normal hadronization process and a hadronization process, where π^0 mesons have intentionally been left stable. A second, less probable, decay channel for neutral pions

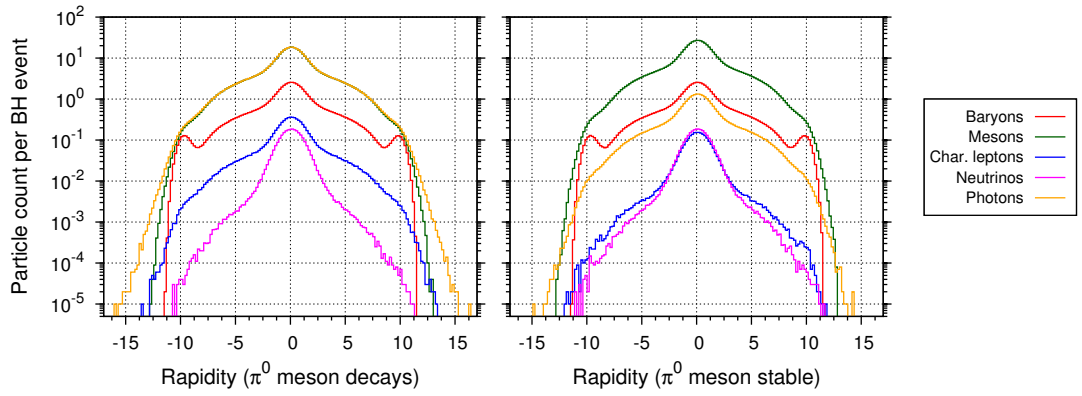

Figure 4.8: Comparison of rapidity histograms for the run from figure 4.6 (left) and equal run with stable π^0 mesons (right). Note the large difference in photon, meson and charged lepton histograms all due to the lack of decay products from decay channels $\pi^0 \longrightarrow \gamma\gamma$ and $\pi^0 \longrightarrow e^+e^-\gamma$.

is $\pi^0 \longrightarrow e^+e^-\gamma$ and has a probability of $\sim 1.1\%$. As a consequence, when π^0 mesons are set to be stable, charged leptons can only come from $\tau^\pm$, $\text{W}^\pm$, Z^0 and η meson decays or if they are already present in the BlackMax output. Since most of these decays will also produce an accompanying neutrino, the two histograms are very similar. Comparing the unstable and stable π^0 histograms in figure 4.8 and taking into account the second decay channel for π^0, uncovers that high–rapidity charged leptons are electrons and positrons, while muons are most commonly just remnants from the initial μBH evaporation.
Another characteristic of the photon spectrum after hadronization and a rather evident difference between PYTHIA and HERWIG is a low–energy tail. These can be sourced to high–energy leptons emitting bremsstrahlung radiation — radiation of a rapidly decelerating particle. In terms of an interaction, we can write it as $e_i^\pm \longrightarrow e_i^\pm\gamma$, where i gives the lepton family. A comparison between enabled and disabled bremsstrahlung radiation is shown on figure 4.9, where a plot from HERWIG has been included, taking into account that HERWIG does not

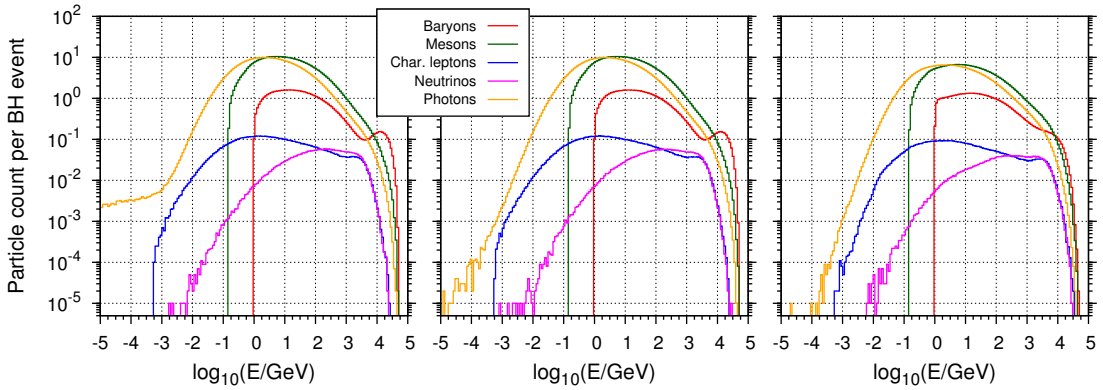

Figure 4.9: Comparison of energy histograms for the run from figure 4.6 (left) and equal run with disabled lepton bremsstrahlung (middle), both taken from the BlackMax/PYTHIA interface. As a further comparison we added the run from HERWIG shown on figure 4.7 (right).

include photon radiation form leptons. If we were to plot other histograms as well, the only noticeable change would be in the p_T histogram, where these low–energy photons turn out to have a low p_T value. After trying to turn off some of the processes during hadronization, we could not find a reason for the large difference in baryons on figures 4.6 and 4.7. The only explanation we could find was that PYTHIA and HERWIG use different hadronization models (string fragmentation model and cluster model, respectively) thus the reason could be hidden there.
For any further simulations, unless otherwise stated, we decided to use PYTHIA to handle hadronization, because of its easier setup with BlackMax. Simulations take about +50% longer, compared to HERWIG, but we get less warnings or event errors. We have excluded all events producing an error from simulations to come, while up to this point we have considered all of the events (PYTHIA encountered no errors, while HERWIG gave a few warnings without stopping the simulation). The only problematic limitation we found is a limit in PYTHIA for the amount of particles it can receive at input. This value is fixed to 80 particles and does not stop the simulation, making results from such events highly doubtful, so we omitted all events giving such warnings henceforth (none were found up to collision energy 100 TeV).
A good comparison between particles coming directly from the μBH and after treating them with hadronization software can be presented using scatter plots, because they present virtually all of the information we can see on histograms we used before. Scatter plots are two–dimensional histograms and adapting the histograming function was as easy as adding another loop to arrange into bins according to counts obtained from two variables. After checking a few scatter plots, we decided that p_Z versus p_T scatter plots held most of the information needed for such a comparison, with p_Z being longitudinal and p_T being traverse momentum of a particle. The reasoning for this is that combining information on p_T and p_Z will uncover information on energy, if we at least know the approximate value of particle mass, and information on rapidity or better yet, the direction of flight for our particles. Figure 4.10 presents such comparisons for all particle groups that have not changed during hadronization — charged leptons (without $\tau^{\pm}$ leptons), neutrinos and photons. The plots are using data already presented in figures 4.5

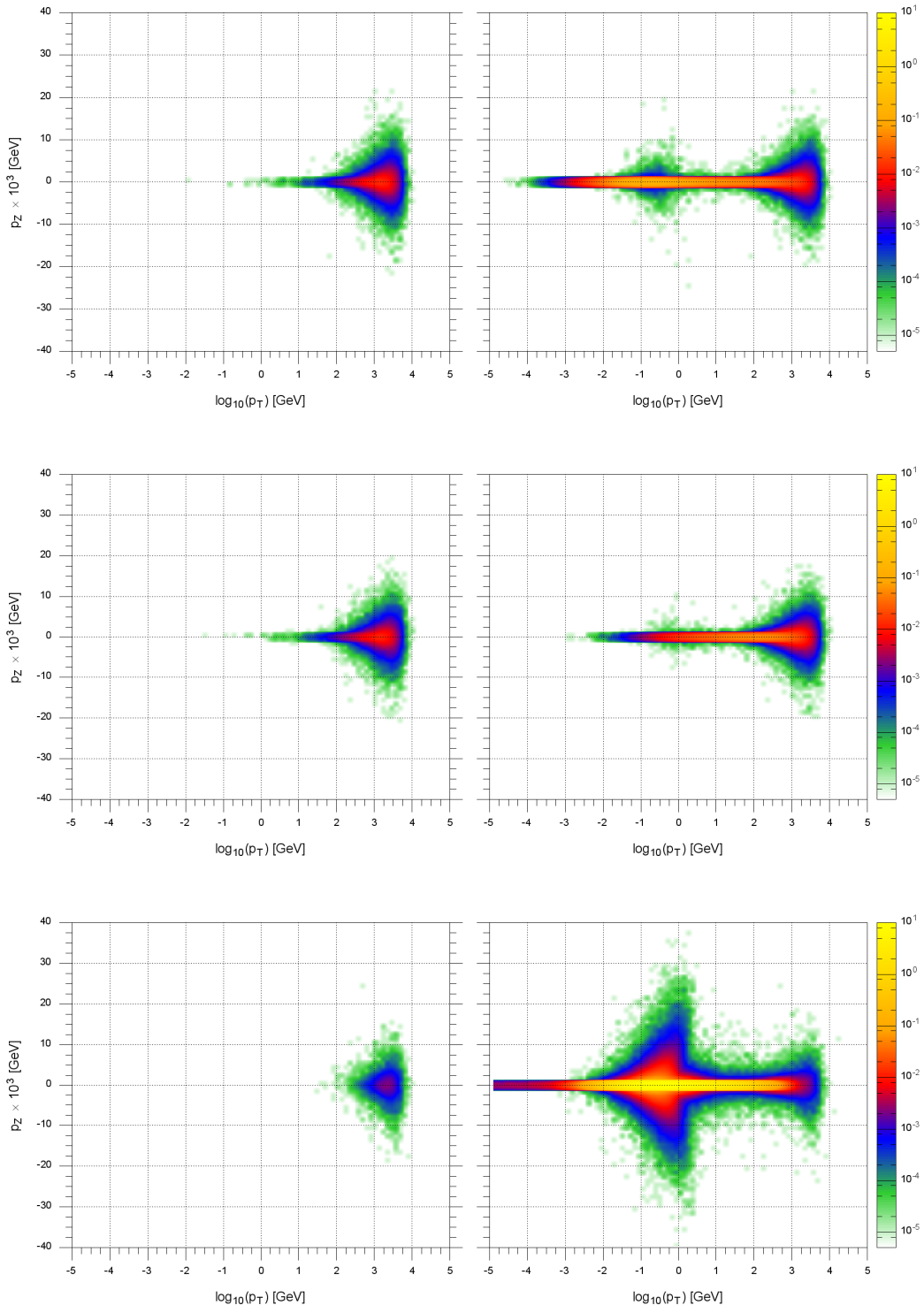

Figure 4.10: Comparison of p_Z/p_T scatter plots before (figures on the left) and after parton shower and hadronization treatment with PYTHIA (figures on the right). Plots only include groups of particles that have not changed during this treatment, going from top to bottom row: charged leptons (without $\tau^{\pm}$ leptons), neutrinos and photons. Data came from simulations already presented in figures 4.5 and 4.6.

and 4.6, obtained from a BlackMax simulation at energy $E_{\mathrm{CMS}} = 100\,\mathrm{TeV}$, $n = 2$ extra dimensions and 10^5 μBH generated events. The first obvious conclusion is that particles with high p_T value and low p_Z value (rapidity close to zero) are mostly just remnants from particles emitted from the μBH. On the other hand, after the hadronization, we see a large number of new particles with low p_T value that are produced during the hadronization process, with photons being most apparent ($\pi^0 \longrightarrow \gamma\gamma$ decay and bremsstrahlung produced low–energy photons). As observed before, when π^0 decayed or was kept stable, the majority of charged leptons with low p_T result from the other channel π^0 will decay to ($\pi^0 \longrightarrow e^+e^-\gamma$).

4.3 Development of extensive air showers

The purpose of this thesis is to find out if micro black holes can be detected in high–energy collisions. Measurements at the LHC have already been done at center–of–mass energy 8 TeV and are still to be performed after the current upgrade at higher energies. However, collisions of ultra–high–energy cosmic rays (UHECR) with the Earth's atmosphere reach much higher energies and are thus prime candidates for μBH detection. A large drawback to using cosmic rays as a detection method for μBHs is due to the fact that the cross sections for a typical cosmic ray collision are on order of 100 mb, whereas μBHs are formed under the μb range (not used in this thesis, as noted in following chapters). Unlike colliders, extensive air showers offer another difficulty, since the direct detection of decay products following the initial collision is impossible with UHECR. There is obviously no such software to simulate a formation of a μBH and the subsequent extensive air shower (EAS) it might produce, but by linking BlackMax and an EAS simulator, some results can be obtained. From a collection of Monte Carlo simulation software, we opted for CORSIKA, the leading software in astroparticle physics with a large collection of options and regular upgrades. It also supports simulations at extreme energies (above $E_0 > 10^{18}\,\mathrm{eV}$), since these would give a better possibility for a μBH to actually form in a collision. Due to the extent of CORSIKA, we will not include a description of its program structure, but only the options and parameters we used or adapted for our simulations.

4.3.1 CORSIKA simulation setup

To accommodate a large variety of experimental setups and possible uses, CORSIKA comes with many options the user can select before creating the final executable program. Most of these rely on the type of primary particles we are interested in and/or a specific way of detecting shower particles produced in an EAS. There is also several possibilities for the treatment of interactions between hadrons and nucleons, consisting of high–energy and low–energy hadronic interaction models, clearly depending on the energy of a particle in the shower. The main purpose of all interaction models is to calculate the mean length a particle will travel before interacting in the atmosphere. For our simulations, we have been using FLUKA [29, 30] as an externally available low–energy hadronic interaction model and QGSJETII–04 [31] model for high–energy hadronic interactions. For comparison purposes, we replaced QGSJETII–04 with Epos–LHC [32] in some of the simulations. All of the mentioned models are fairly demanding in terms

of computing memory and time, but running the software on a GRID, allowing parallel treatment of simulations, took care of all these drawbacks and sped up calculations. Additionally, we also selected slanted longitudinal distribution, thinning and stack input options.
The slanted longitudinal distribution option produces a longitudinal shower profile in terms of an inclined range of depth (profile along the shower axis) instead of using vertical atmospheric depth. Crossing from one to the other is simple and can be done with

$$d_{\text{vertical}} = d_{\text{inclined}} \cdot \cos\theta, \tag{4.10}$$

where θ is the inclination angle of the shower (the zenith angle). This option is mostly cosmetic, but it does simplify setting the bin interval sizes for inclined showers. For example, setting the bin size to a fixed value using the slanted option will give comparable profiles in terms of depth for vertical and inclined showers. Furthermore, if we decide to switch to vertical depth with equation (4.10), we would get a denser collection of bins, improving measuring points and thus the final curve fit.
The second option, thinning [33], is an important option for showers with primary particle energies higher than $10^{16}\,\text{eV}$, because tracking each particle separately would give an enormous increase in simulation time. Therefore, particles with energy smaller than E_{thin} are treated collectively by only following one of them and assigning a weight to it, while dropping all the rest. CORSIKA remembers the assigned weights and according to statistic probability recreates any dropped particles for the final particle listing or measurement points in–between. Thinning energy is defined through a thinning fraction

$$\epsilon = \frac{E_{\text{thin}}}{E_0}, \tag{4.11}$$

where E_0 is the energy of a primary particle. This fraction is set depending on the strength of thinning we want, with reasonable values of $\epsilon \sim 10^{-6}$ at extreme energies.
The last option we decided to use was the stack input, a special kind of input of particles that skips the primary particle and uses secondary particles instead. This is extremely useful when we do not know the identity of a primary particle or if it is an exotic particle that can not normally be used as input to CORSIKA. It certainly qualifies when treating formation and emission of μBHs in proton collisions with atmospheric molecules. A specific input file needs to be created listing all secondary particles, their types, energies and momenta and the energy of the primary particle. There is, however, a drawback to the stack input option supplied with CORSIKA. The first interaction depth (where a primary interacts with the atmosphere) needs to be predetermined, unlike a normal simulation with a primary particle, where this is to be randomly calculated depending on the cross–section. We addressed this issue and adapted CORSIKA to randomly determine the first interaction depth for stack input, described in section 4.3.3.
For each simulation run we need to provide additional parameters called steering keywords, that mainly have to do with primary particle definitions, atmosphere selection, geocoordinate positioning and settings for options we selected for our CORSIKA run. Similar to BlackMax, we will only describe some of the ones we were using for our purposes, whereas a full definition for all possible parameters

can be found in [34].
For a simulation with a primary particle, we need to define its type, primary energy E_0 and the slope of the primary energy spectrum (shown in figure 2.1), while a simulation with stack input only needs the listing of secondary particles to run. We kept the energy of a primary particle constant for better comparison with μBH induced runs, so the setting of the spectrum slope was not necessary. The direction of flight of a primary particle is selected by setting zenith θ and azimuth ϕ angles, with a graphical representation of the coordinate system shown on figure 4.11. The axes should not be confused with the ones used in BlackMax, where longitudinal momentum was designated with p_Z and the two components of the traverse momentum p_T as p_X and p_Y. Depending on the depth at which

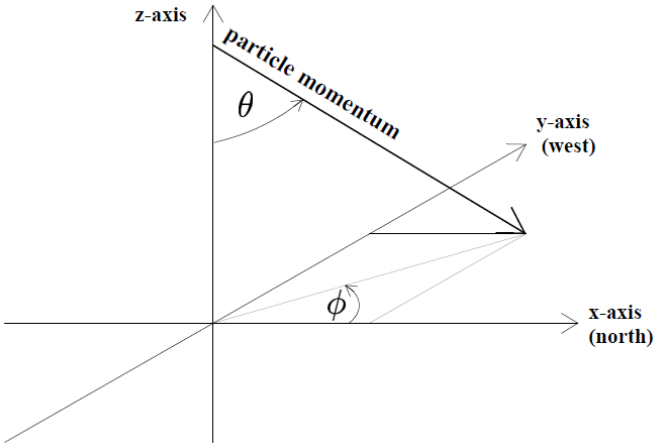

Figure 4.11: The internal coordinate system used by CORSIKA. θ is the zenith angle and ϕ is the azimuth angle (figure ref. [34]).

first interaction occurs, we could also define a fixed depth of first interaction, but we let CORSIKA calculate this randomly according to cross–section values for a primary interaction with the atmosphere. Next, we have parameters describing the properties of the atmosphere, the Earth's magnetic field and the height of our selected detector. We set the magnetic field to an average value for the location of the Pierre Auger Observatory (PAO, Malargüe), taken from the online magnetic field calculator Geomag [35]. The choice of an atmospheric model was not important, because we decided to display all results in units of $\mathrm{g\,cm^{-2}}$, that remain equal regardless of the selected model. We placed the detector at sea level to get a longer path for showers to develop, because selecting the PAO detector elevation stops the sampling for longitudinal profiles too early to observe muon profile features. Thinning in all of our simulations was set a fractional value of $\epsilon = 10^{-6}$ and an energy cut–off of 0.3 GeV for hadrons and muons and 0.003 GeV for electromagnetic particles (not including muons) was used. Below the cut–off energy values particles are no longer being followed in the current simulation in order to save on resources and simulation time. The transition value between high–energy and low–energy hadronic models tells CORSIKA to switch from one to the other at a predetermined energy value, that we kept at 80 GeV.

4.3.2 Preparing particles for CORSIKA stack input

Each particle after the hadronization process is defined by its type, energy and momentum. They are given in the center–of–mass frame of reference, with values E_{CMS}, p_X, p_Y and p_Z. The forward direction in the BlackMax coordinate system is the positive Z–axis. However, due to the difference between BlackMax and CORSIKA coordinate systems, we will be using notation p_L, standing for longitudinal and p_{TX} and p_{TY} for traverse momentum components, so the definitions of coordinate axes are equal for both programs. According to the theory of special relativity, when making a change from a center–of–mass frame to the laboratory frame, only longitudinal components of physical quantities will get affected, i.e. the quantities parallel to the motion of the frame. A way to imagine both reference frames is to think of the center–of–mass frame as a stationary frame between both particles, waiting for them to collide at its origin. A laboratory frame would then just need to be moving towards the first particle, so that the second particle seems to be stationary in this frame. The second particle here is considered as the atmospheric molecule, with a reasonable assumption that it is stationary — Brownian motion is considerably smaller than the motion of the incoming particle. According to this little thought experiment figure 4.12 displays the general idea behind it. From the schematic, we see that unprimed quantities belong to

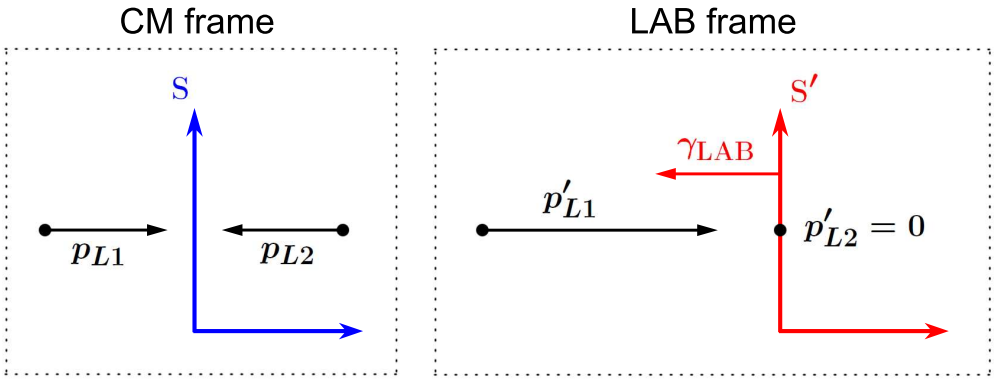

Figure 4.12: A schematic representation of center–of–mass and laboratory reference frames. Unprimed quantities belong to the center–of–mass frame and primed quantities to the laboratory frame. γ_{LAB} defines the Lorentz factor for the movement of frame S′. For clarity, the origins of both frames have been shifted a bit lower.

the center–of–mass frame (frame S), while primed ones describe quantities in the laboratory frame (frame S′). The frames will henceforth be denoted as frame S and frame S′, accordingly. All of the following equations will be written using natural units, where $\hbar = c = 1$ and energy, momentum and mass all have units of electron–volt (eV). Along the lines of special relativity, momentum and energy are connected analogously to space and time, thus we can write the same rules for Lorentz transformations of these

$$E' = \gamma \cdot E - \beta\gamma \cdot p_{\parallel},$$
$$p'_{\parallel} = \gamma \cdot p_{\parallel} - \beta\gamma \cdot E,$$
$$p'_{\perp} = p_{\perp},$$

where $p_\parallel$ gives the parallel component and $p_\perp$ gives the perpendicular component of momentum to the direction of motion of frame S′. There are some general properties for each of these frames of reference, that we will be needing in further calculations. In frame S, collision particles will always have equal energies ($E_1 = E_2$), with their sum being the center–of–mass energy $E_{\mathrm{CMS}} = E_1 + E_2$. Furthermore, if both particles have equal mass, their longitudinal momenta are equal and opposite ($p_{L1} = -p_{L2}$). In frame S′, on the other hand, one of the particles is at rest, thus $E'_2 = m_2$ and $p'_{L2} = 0$. In our case, frame S′ is moving towards frame S, which gives us a plus sign instead of a minus in the first two equations. We can also use our notation $p_\parallel = p_L$ and $p_\perp = p_T$ and replace β with

$$\gamma = \frac{1}{\sqrt{1-\beta^2}} \quad \longrightarrow \quad \beta = \frac{1}{\gamma}\sqrt{\gamma^2 - 1}. \tag{4.12}$$

Rewriting the Lorentz equations for our situation and dropping the equation with perpendicular components gives us

$$\begin{aligned} E' &= \gamma_{\mathrm{LAB}} \cdot E + \sqrt{(\gamma^2_{\mathrm{LAB}} - 1)}\, p_L, \\ p'_L &= \gamma_{\mathrm{LAB}} \cdot p_L + \sqrt{(\gamma^2_{\mathrm{LAB}} - 1)}\, E. \end{aligned} \tag{4.13}$$

The missing Lorentz factor γ_{LAB} is simply just the γ of the second particle in frame S — only in that situation would the second particle be at rest in frame S′. We can write it in terms of its energy and mass as

$$\gamma_{\mathrm{LAB}} = \frac{E_2}{m_2}. \tag{4.14}$$

The procedure of transforming output particles from the BlackMax/PYTHIA interface to the laboratory frame involves firstly calculating the Lorentz factor γ_{LAB} of the initial collision from equation (4.14) and secondly using it with equations (4.13) and their center–of–mass values of energy E and momentum p_L to get the needed values of E' and p'_L for each of the emitted particles. When comparing results in the laboratory frame with those in the center–of–mass frame, we obtain a good approximation for energy transformation [28], as follows:

$$E_{\mathrm{LAB}} = \frac{E^2_{\mathrm{CMS}}}{2m}, \tag{4.15}$$

where it is assumed that both particles are of equal type and particle mass m is small compared to particle energy E.
A stack input file, filled with a listing of particles we want to input to CORSIKA, looks like:

```
 10   1.0000000e+12
   1   14   1.6666282e+11   1.6666282e+11  -2.6428071e-01  -6.9273949e-02
   2    8   1.4601226e+11   1.4601226e+11   1.4363861e-01  -2.0616763e-01
   3    1   1.2186336e+11   1.2186336e+11   5.0799690e-02   2.7843537e-01
   4    8   7.1118603e+10   7.1118603e+10  -7.6660475e-02  -1.1112961e-02
   5    9   5.2391532e+10   5.2391532e+10  -2.1356409e-01   2.7667498e-01
   6    9   4.6533380e+10   4.6533380e+10   2.4587253e+00  -3.3794748e+00
   7    9   3.8439969e+10   3.8439969e+10   1.0094342e-01  -5.4806577e-02
   8   25   3.5822180e+10   3.5822180e+10   2.3919497e+00  -2.9103469e+00
   9    8   2.8085349e+10   2.8085349e+10   1.5632968e+00  -1.3159003e+00
  10   13   2.5977850e+10   2.5977850e+10   2.8248311e+00  -3.0209840e+00
```

The first row gives a complete number of particles in the file and the energy of the primary particle in GeV. For this example, only 10 highest energy particles were selected from a BlackMax/PYTHIA run with collision energy $E_{\mathrm{LAB}} = 10^{21}\,\mathrm{eV} = 10^{12}\,\mathrm{GeV}$ (in the center–of–mass frame, this is roughly $E_{\mathrm{CMS}} = 1400\,\mathrm{TeV}$). The first column holds sequential numbers for particles, while the second holds particle IDs according to the CORSIKA particle numbering scheme, explained in appendix Appendix B. The last four columns give information on the particle energy E, longitudinal momentum p_L and both components of the traverse momentum p_T, respectively. Although, the above example only lists a short collection of particles, the real range of energies we are dealing with is as much as 10 orders of magnitude. This is illustrated on figure 4.13, where the energy histogram depends on the number of highest energy particles we select for a stack input simulation. The particles were selected from the highest energies to the lowest energies, with

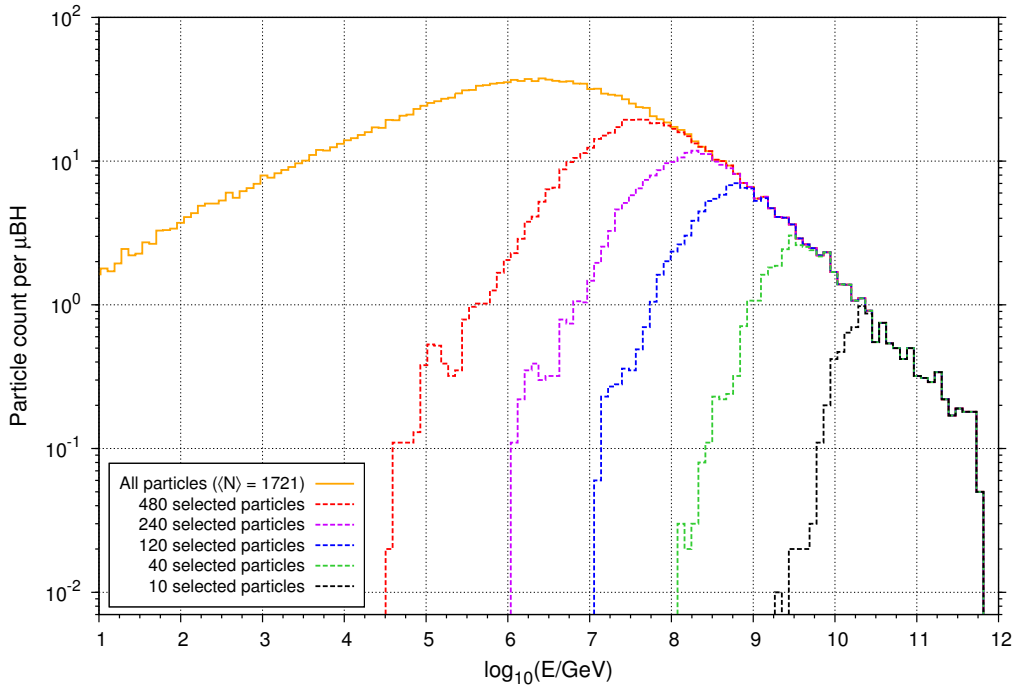

Figure 4.13: Energy histograms of particles that remain stable after treatment with the BlackMax/PYTHIA interface, with variable thresholds on the number of particles. The particles were selected by their energy, from highest to lowest energy, taken from 100 events at collision laboratory energy 10^{21} eV.

sets of 10, 40, 120, 240 and 480 particles, presented with dashed lines. A final histogram, displayed with a solid line, spans over a complete range of energies and consists of all stable particles, with an average number of 1721 particles per event from 100 events. Each of these possibilities has been taken as input for an EAS simulation, together with two extra sets of 20 and 60 particles not displayed on figure 4.13. For the actual simulations, we have always taken into account that a single μBH event produces a single EAS, thus whenever mentioned, 100 events means exactly the same as 100 showers, just that one corresponds to BlackMax simulations and the other to CORSIKA driven simulations. The simplest way to get some characteristics of a shower is by examining its longitudinal profile, displaying the number of particles or their normated values depending on the amount

of atmosphere a shower has already crossed (along the shower axis). This value is known as depth with units $\mathrm{g\,cm^{-2}}$, making it extremely useful, because it is independent from the atmospheric density. As a rule, depth is usually meant as the travelled depth, therefore a value of $0\,\mathrm{g\,cm^{-2}}$ will correspond to the top of the Earth's atmosphere. Figure 4.14 displays such a longitudinal profile for the cases where we made a selection from the particles emitted by a μBH. For the sake of

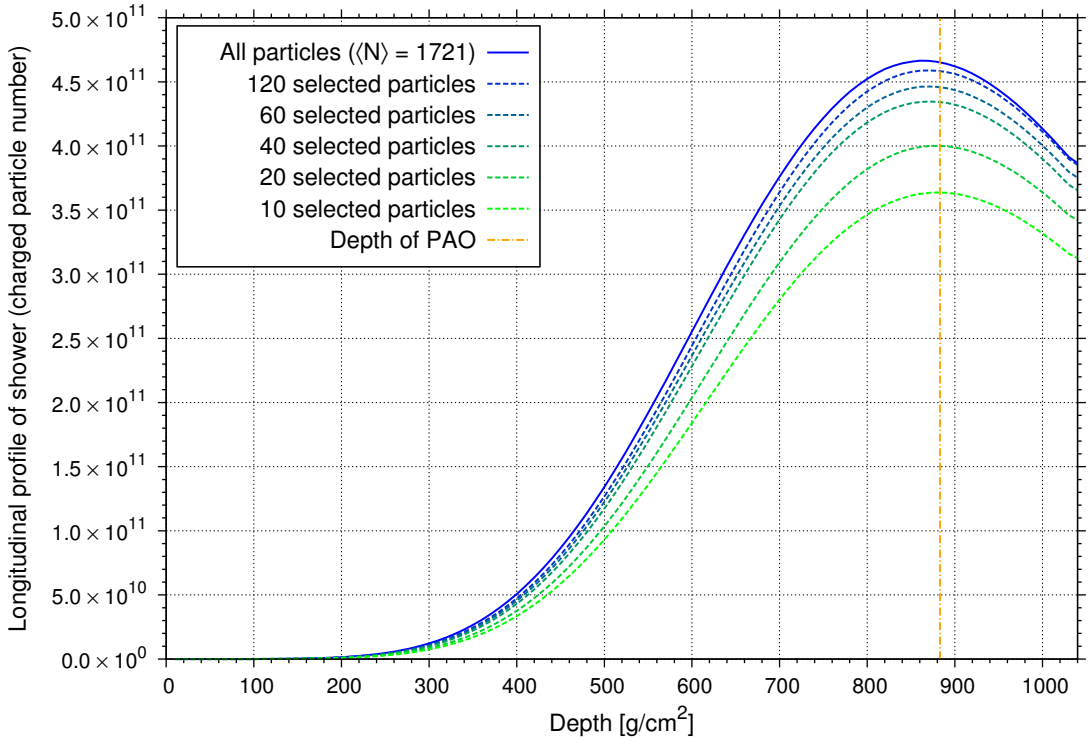

Figure 4.14: Comparison of longitudinal profiles for charged particles depending on the number of particles we select for stack input. For clarity, sets with 240 and 480 particles have been replaced with simulations with 20 and 60 particles. As a reference point, the line corresponding to the depth of the Pierre Auger Observatory has been added ($883\,\mathrm{g\,cm^{-2}} \approx 1400\,\mathrm{m}$ a.s.l.). Results taken from 100 showers at energy $10^{21}\,\mathrm{eV}$ with a fixed first interaction height.

clarity, we did not use all sets of particles, but only the sets including 10, 20, 40, 60 and 120 particles, with an included longitudinal profile for a simulation with all stable input particles and the depth of the Pierre Auger Observatory (PAO). The simulated shower was set to be vertical, therefore the depth of PAO corresponds to roughly $883\,\mathrm{g\,cm^{-2}}$ (1400 m a.s.l.). The most recognizable feature of a longitudinal profile is by far its maximum value of particles denoted with X_{max} and tightly related to primary particle type and energy. A more detailed explanation of X_{max} follows in chapter 5. It is easily seen that profiles on figure 4.14 have a different depth of shower maximum, obviously resulting from the number of particles we used for input, especially since we fixed the first interaction depth for all simulations. Fitting the longitudinal profile with a Gaisser–Hillas curve, again described in detail in chapter 5, gives the value of X_{max} as one of the parameters. Taking the results displayed in figure 4.14, we plotted X_{max} in terms of the number of selected particles to estimate the trend and the most probable limiting value.

This is displayed on figure 4.15, where $X_{\max}$ values are shown as blue dots with error bars in the direction of the y–axis. The red line is the best fit we could find

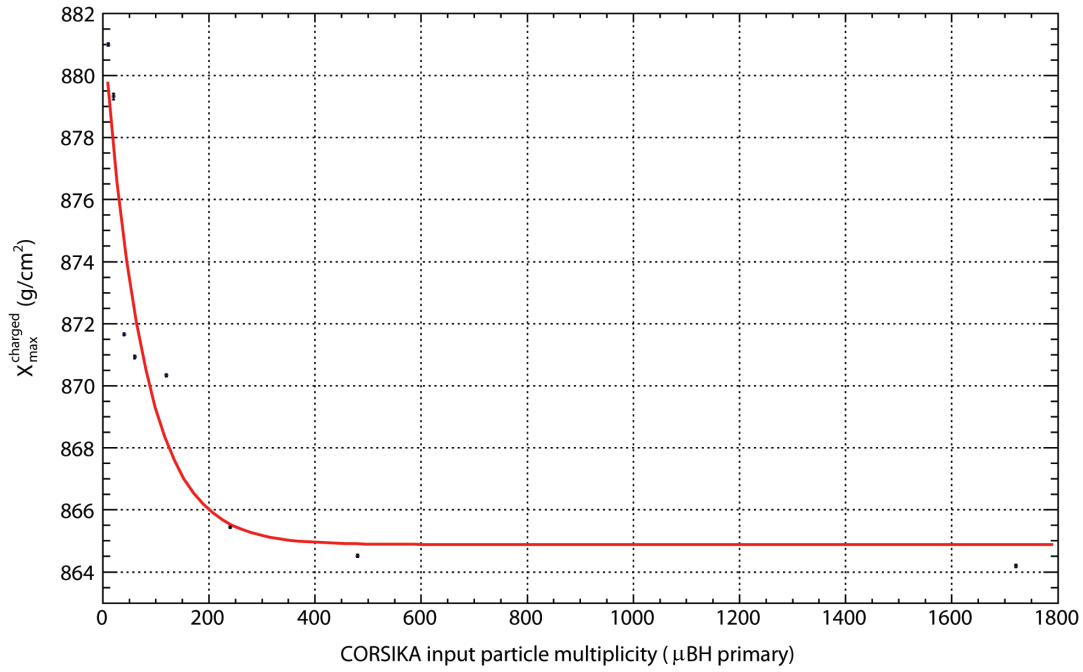

Figure 4.15: Depth of shower maximum for charged particles $X_{\mathrm{xmax}}^{\mathrm{charged}}$ in terms of the number of particles we select for stack input. Blue points and error bars correspond to $X_{\mathrm{xmax}}^{\mathrm{charged}}$ values from fitting longitudinal profiles on figure 4.14. The red line is the best fit to the gathered points, described by function (4.16).

through the given points and their errors by using a function

$$f(x) = a\,\mathrm{e}^{bx} + c, \tag{4.16}$$

where a, b and c are parameters defined during the fitting process. In this particular fit, these turned out to be

$$\begin{aligned} a &= 16.84\,\mathrm{g\,cm^{-2}} \pm 5.83 \times 10^{-2}\,\mathrm{g\,cm^{-2}}, \\ b &= -1.35 \pm 1.39 \times 10^{-4}, \\ c &= 864.88\,\mathrm{g\,cm^{-2}} \pm 3.13 \times 10^{-2}\,\mathrm{g\,cm^{-2}}. \end{aligned}$$

Therefore, $864.88\,\mathrm{g\,cm^{-2}}$ is the estimated limiting depth, where a shower with all of the emitted particles from μBH taken as stack input for an EAS simulation and laboratory collision energy 10^{21} eV will have a shower maximum.
The shift of $X_{\max}$ in above simulations is a good indication that a larger number of secondary particles means a quicker rise of a longitudinal profile up to its maximum value. Although the differences in $X_{\max}$, according to figure 4.15, are at most $\sim 2\%$ and we would not produce a considerable error by taking one of the sets of particles, we decided to use all particles for stack input in further simulations. This does extend the time it takes to finish the simulations considerably (there is a 30% increase, if comparing a simulation with a set of 10 selected and all particles), but for the aim of this thesis it was much more important to obtain qualitative results, while quantitative results could be obtained in future work.

4.3.3 Extensive air shower first interaction depth

First interaction depth is the point in the Earth's atmosphere, where an incoming cosmic ray or primary particle produces an initial collision with air molecules. This is the actual start of an air shower, because secondary particles are created in the collision, the first steps in a larger cascade of particles. The depth is difficult to determine experimentally, primarily due to the lack of information on the type of the primary particle and a not inconsiderable error on primary energy. However, when it comes to Monte Carlo simulations we can describe collision processes through the cross–section of an interaction and by using different primary particles and varying energies, we can distinguish shower properties resulting from our choice. CORSIKA calculates the cross–sections, depending on the high–energy hadron interaction model we are using, and from them the first interaction depth. This depth includes a random factor that gives us more of a statistical probability for the interaction, as expected in reality. It is calculated by using

$$X_0 = \frac{-\ln(R) \cdot m_a}{N_A \cdot \sigma(E)}, \tag{4.17}$$

where R is a random number on the interval $(0, 1)$, $m_a = 14.543\,\mathrm{g\,mol^{-1}}$ is the average air molecular weight, $N_A = 6.0221 \times 10^{-4}\,\mathrm{cm^2\,mb^{-1}\,mol^{-1}}$ is the Avogadro constant converted for the use of cross–section $\sigma(E)$ in units of millibarn (mb). The resulting depth X_0 then has the familiar units of $\mathrm{g\,cm^{-2}}$. For nucleons, i.e. protons and neutrons, the energy used in equation (4.17) is just the particle's laboratory energy $E = E_0$. However, for composite heavier primaries, such as iron, the energy we are using for the calculation of cross–section is the energy per nucleus, defined as

$$E_{\mathrm{nuc}} = \gamma \frac{m_p + m_n}{2} = \frac{E_0}{2} \frac{m_p + m_n}{m_{\mathrm{prim}}}, \tag{4.18}$$

where γ is the Lorentz factor of the primary, E_0 is the primary energy and m_p, m_n and m_{prim} are proton, neutron and primary particle masses, respectively. For comparison purposes, figure 4.16 displays cross–section σ in terms of primary energy E_0 for protons and iron primaries as calculated using CORSIKA in conjunction with the QGSJETII–04 high–energy hadron interaction model. The energy per nucleon for iron, with mass $m_{\mathrm{Fe}} = 52.582\,\mathrm{GeV}$, is equal to $E_{\mathrm{nuc}} = E_0 \cdot 1.786 \times 10^{-2}$. However, the stack input option in CORSIKA is meant to be used for exotic particle interactions not covered by internal calculations, thus assuming that we will be supplying it with a fixed depth of first interaction. This is also valid for μBHs, though due to its small production cross–section, compared to the first interaction in normal EAS, we decided to use the existing way CORSIKA calculates the cross–section and first interaction depth. That way we gave a μBH induced EAS the best chance of actually forming in the atmosphere. The assumption is therefore that a primary proton interacts with air molecules in the atmosphere in a normal way and then produces a μBH, instead of continuing to secondary particles straightaway. Adopting the same way of calculating the first interaction depth, as for a case with a primary proton, was done just by permitting CORSIKA to use the same first interaction depth calculation function for a simulation with stack input enabled. This also meant that some of the error checks had to be disabled, but the end result was promising. Figure 4.17 shows histograms for first interaction depth of

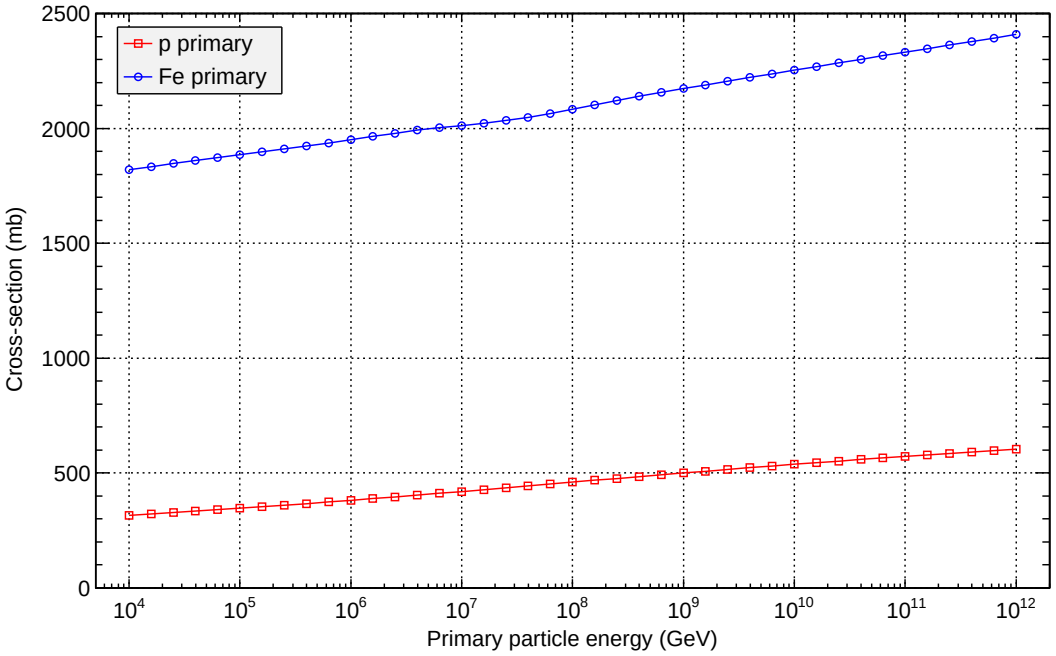

Figure 4.16: Comparison of cross–section in terms of primary energy E_0 for proton (red) and iron (blue). The high–energy interaction model used in this plot is QGSJETII–04.

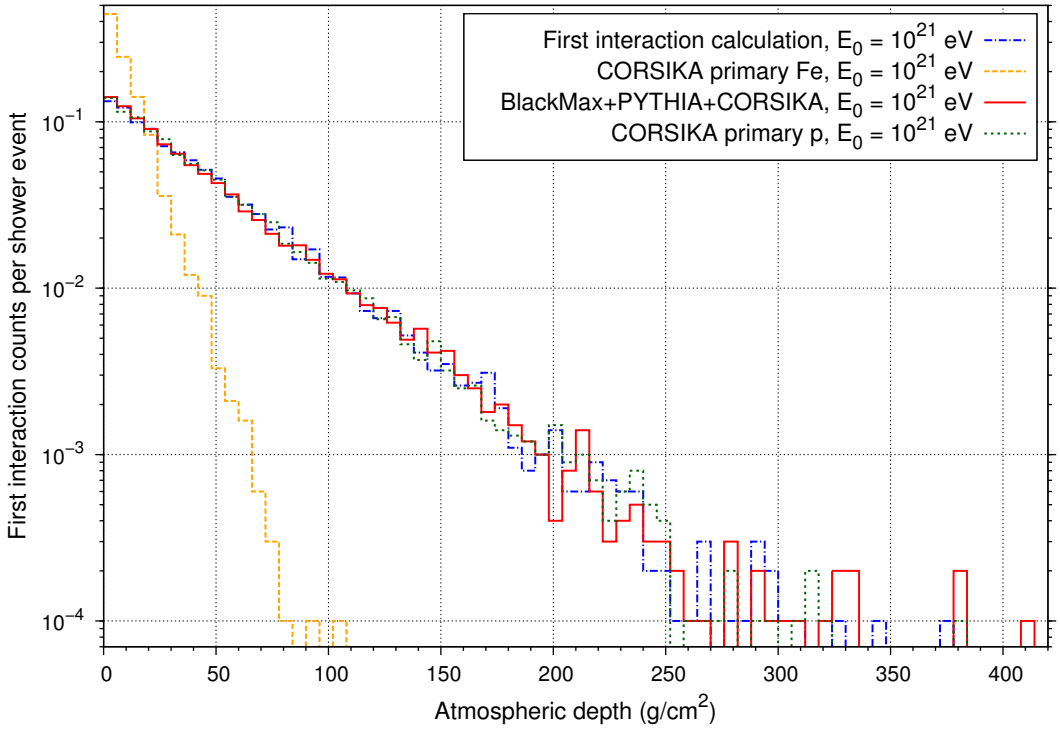

Figure 4.17: First interaction depth distribution comparing the analytic formula of equation (4.17) (blue) and the actual Monte Carlo predictions from the simulation of 10^4 EAS for a proton primary (green), a μBH mid–stage (red) and an iron primary (orange). The y–axis has been normated to display counts per shower. Note that a value of 10^{-4} means that the primary in only one out of 10^4 showers encountered an interaction at that depth.

a proton primary shower, a shower with a μBH intermediate stage, a calculation from equation (4.17) and an iron primary shower for comparison. The difference seems to be bigger at larger depths, but combining the fact that the y–axis is in logarithmic scale and the random number seeds are different, we can conclude that first interaction depth is similar in all three cases, where an initial collision of proton and air is present. Keep in mind that a histogram value of 10^{-4} relates to a single count out of 10^4 showers. We decided to include the first interaction depth histogram for iron, which clearly shows that iron primaries with their much larger cross–section will interact earlier in the atmosphere ($X_0 \propto \sigma(E)^{-1}$) than protons, shifting the histogram to smaller depths.
All further simulations of μBH induced showers use this way of determining the first interaction depth, instead of keeping it fixed. This produces a more statistical way of describing the collision process and includes the proton–air initial interaction. On the other hand, all simulations with a primary particle (proton, iron or photon) that do not produce a μBH have remained unchanged and receive the usual CORSIKA treatment.

5 Results

The main scope of this thesis is to compare a μBH induced EAS to showers started by various primary particles and evaluate the possibility of distinguishing them with present experimental setups. As mentioned in the previous chapter, a longitudinal profile is a simple way of examining characteristics of an air shower. It represents the number of particles produced in a shower in terms of depth, measured along the shower axis. Apart from its most recognizable feature, the depth where a shower gets to the maximal number of particles $X_{\max}$, we can also get some information on primary particle type from the leading edge rise and the amount of muon content in a shower. Naturally, when it comes to comparing simulation results with those obtained from experiments, only charged particles are considered, because these are the only ones that are detected in most experiments. As an example, large–extent surface detector arrays are mostly based on Cherenkov light detection, where a high speed charged particle causes light to be emitted, inducing a sizable signal through photomultiplication.
Other features of the longitudinal profile are the already mentioned first interaction depth X_0 and the number of particles at shower maximum $N_{\max}$. A longitudinal profile in a CORSIKA simulation is measured at equal depth intervals that can be set at the beginning of each run and need to be carefully selected. A fine resolution might give us great statistics, when determining features from a longitudinal profile, but they come at a price of increased simulation time. To still have good statistics, we used sampling at depth segments of $10\,\mathrm{g\,cm^{-2}}$. However, to gain profile parameters with small error values, a fit with a suitable function is necessary. The most viable and detailed function for such a fit has been introduced by Gaisser and Hillas [36], describing the longitudinal profile

$$N(X) = N_{\max}\left(\frac{X - X_0}{X_{\max} - X_0}\right)^{\frac{X_{\max}-X_0}{\lambda}} \exp\left[\frac{X_{\max} - X}{\lambda}\right], \tag{5.1}$$

where λ is the shower decay length, while X_0, $X_{\max}$ and $N_{\max}$ are first interaction depth, shower maximum and the number of particles at shower maximum ($N_{\max} = N(X_{\max})$), respectively. First interaction depth is determined during simulations and is therefore a known quantity, but fitting with a fixed X_0 returns a poorer fit than leaving it as a free fitting parameter. We have therefore decided to leave it free, since there is no use in obtaining it from the fit, because it can be extracted directly from simulations. For this thesis, the value of λ is not important and was unbound to give the best possible fit on $X_{\max}$. Longitudinal profiles for muons have a unique behavior at larger depths, with an inflection that can not be accounted for using the Gaisser–Hillas function. Therefore, fitting these adds an additional challenge, where a possible solution is to restrict the fitting range in the vicinity of the shower maximum. Figure 5.1 presents two distinct fitting ranges and their residuals, assessing the goodness of each fit.

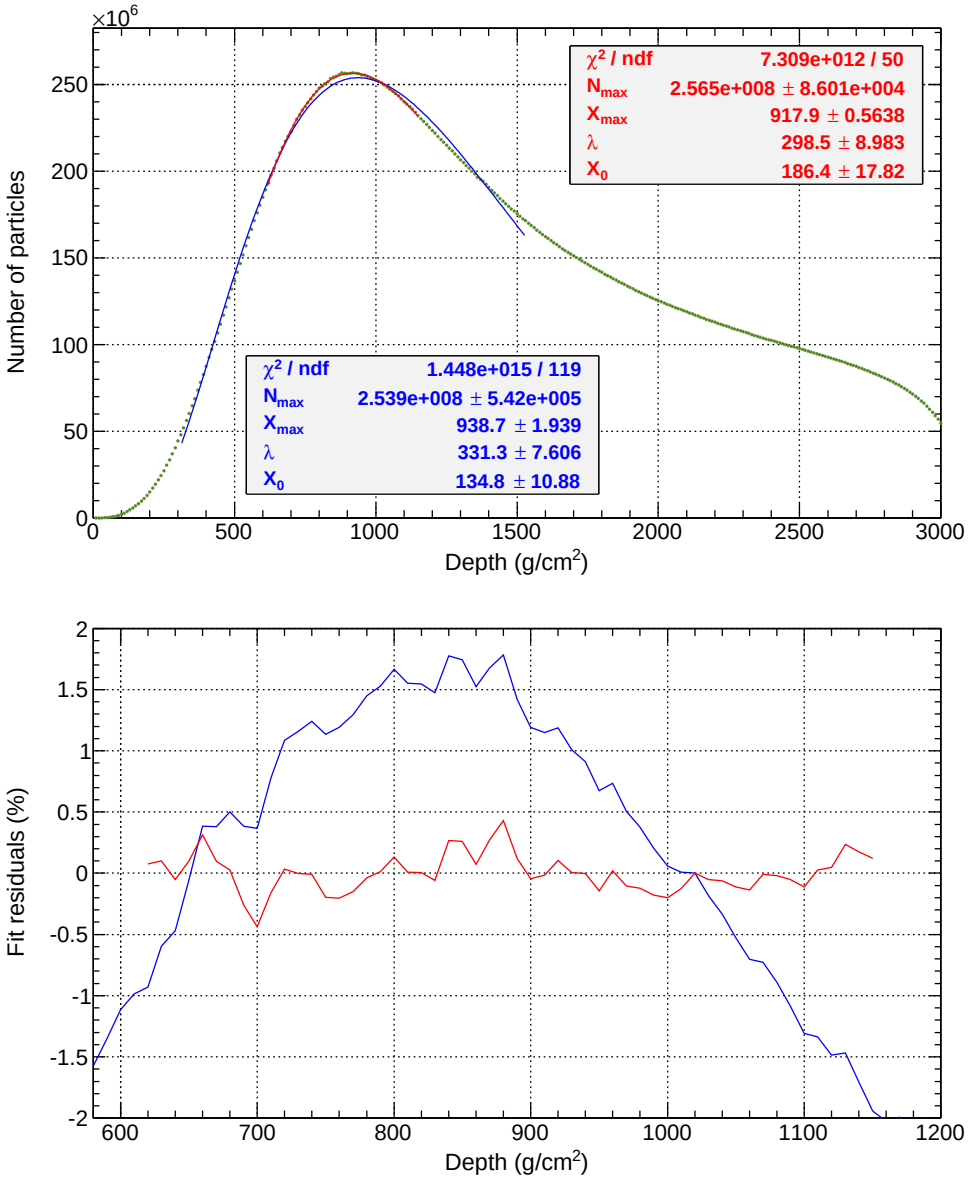

Figure 5.1: Fitting of a muon longitudinal profile using function (5.1) with ranges $[{}^1\!/_3 X_{\max}, {}^5\!/_3 X_{\max}]$ (blue fit) and $[{}^2\!/_3 X_{\max}, {}^5\!/_4 X_{\max}]$ (red fit). The plot on the right shows residuals for both fits near shower maximum. The problematic region after shower maximum was left out from the fit.

Looking at fitting results and the residuals, it is apparent that narrower interval produces quite an improvement on determining the four parameters and keeping vertical deviations within 0.5% around $X_{\max}$. Selecting an even smaller fitting range would further improve our margin of error, but we felt that this could lead to unforeseen errors due to a small number of fitting points. Fits were therefore done inside the interval $[{}^2\!/_3 X_{\max}, {}^5\!/_4 X_{\max}]$. Longitudinal profiles for charged particles, on the other hand, do not produce any loose fits with a larger range, but for the sake of continuity, we used the same fitting procedure. The process of fitting longitudinal profile data from multiple simulations with equal initial settings and creating an average longitudinal profile took the following path:

1. Longitudinal profile data from multiple simulations are considered separately

and the fit with function (5.1) performed on each of these individually.

2. An average longitudinal profile is constructed by summing up individual shower profiles and normating to the number of showers.

3. Fit parameters obtained through step 1 are also given an average value by summing them and dividing with the number of showers. The errors on parameters are treated the same way.

For a handful of shower profiles, fitting procedure did not converge, therefore the range was slightly increased or decreased to a maximum of ±5% deviation from initial fit boundary conditions. In case changing the fitting range does not produce a convergent fit, these simulations were dropped before final average calculations. In most cases, the non–convergent fits were due to double peaks in longitudinal profiles. Any of such unused runs are mentioned when displaying results.
To reduce the number of simultaneous GRID simulations, 100 showers were performed for each set, which is, statistically speaking, far from ideal, but it does iron out some of the larger fluctuations in depths of first interactions and profile evolution. For a better representation, figure 5.2 shows separate longitudinal profiles for charged particles and muons. We chose a 70° inclination to let the EAS run well

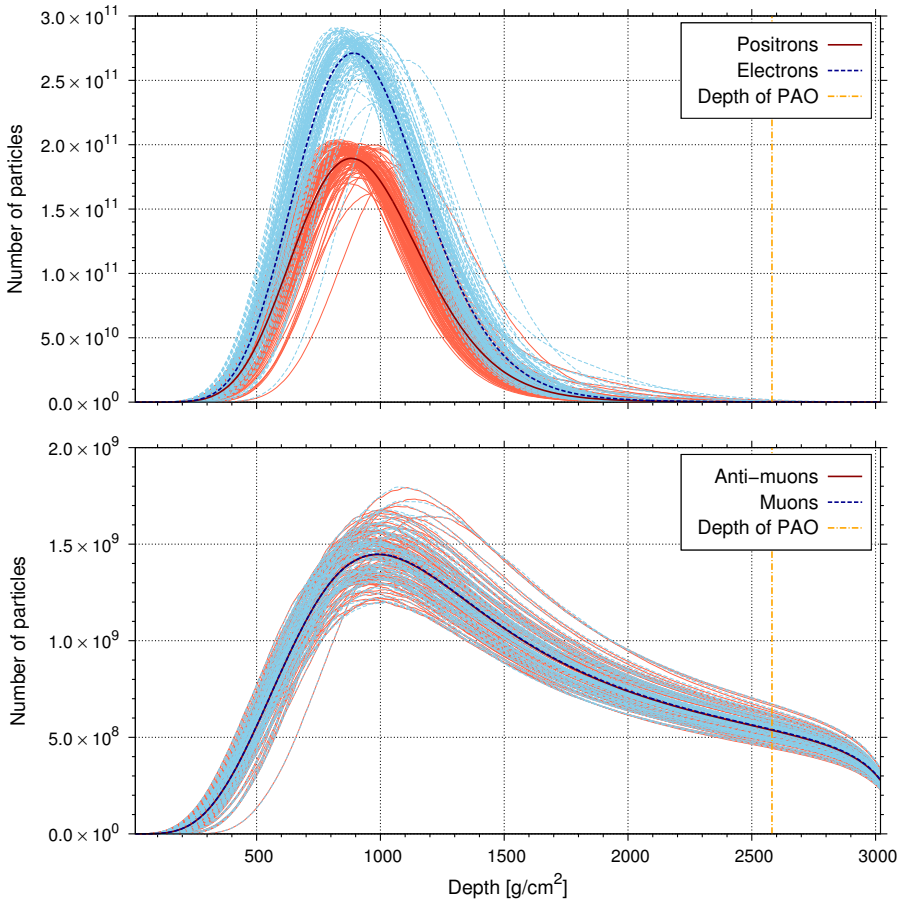

Figure 5.2: Longitudinal profiles of showers for positrons, electrons, anti–muons and muons, with their average values displayed with thicker lines. Results were obtained from a run of 100 showers with a primary proton at $E_0 = 10^{21}$ eV and a $\theta = 70°$ inclination. Depth of the Pierre Auger Observatory is added for comparison (due to a slanted shower, its depth is $2582\,\mathrm{g\,cm^{-2}}$).

past its depth of maximum, since in a vertical shower the muon maximum would happen near or below sea level, thus making it hard to distinguish most features of an EAS and creating a large error on $X_{\max}$ during fitting.
The first part of simulations consisted of comparisons between primary particle types, including the μBH intermediate stage, and their energies on a range between 10^{18} eV and 10^{21} eV. This covers the range of ultra–high energy cosmic rays (UHECR), the main aim of observations at large surface arrays like the PAO surface detector array. High–energy interactions were handled by QGSJETII–04, while FLUKA took care of low–energy interactions, switching between the two at 80 GeV. Thinning was active throughout and kept constant to a fraction of $\epsilon = 10^{-6}$ to ensure similar treatment of each run. In the same sense, energy cut–offs were set to 0.3 GeV for hadrons and muons and 0.003 GeV for the rest of electromagnetic particles. The simulations were split into four sets, each set at a different primary particle energy 10^{18} eV, 10^{19} eV, 10^{20} eV and 10^{21} eV. A set then compares four possible starting situations, namely, a proton primary with a μBH intermediate stage, and the usual primary particle treatment, where proton, iron and photon were used as primaries. Showers with primary proton and iron are both hadron type showers, meaning they are nearly impossible to distinguish in observations, due to similarities in interaction processes. The difference is in their interaction cross–sections, resulting in a quicker rise to the depth of maximum for iron primaries. On the other hand, primary photons have weaker interactions with the atmosphere, thus creating less extensive showers, a property typical for electromagnetic showers. Average longitudinal profiles for charged particles and muons from all four sets are displayed on figures 5.3 and 5.4, respectively. Viewing both charged particle and muon longitudinal profiles at the same time, clearly reveals that photons are completely independent, due to their electromagnetic EAS, and can be eliminated from further comparisons with showers containing a μBH intermediate stage. However, both proton primaries and iron primaries are viable contenders for the comparison, with longitudinal profiles of μBH induced EAS somewhere in–between the two. What is even more interesting, is that the longitudinal profile for a μBH shower closely resembles the one with an iron primary at lower energies, but at higher energies it shifts towards more of a proton induced case instead. To really understand why this shift occurs, we need to investigate the distribution of energy amongst particle types. In the case of a proton primary, a single nucleon carries all of the starting energy of a shower, transferring it to secondary particles that continue evolving the EAS. Contrarily, an iron primary is constructed from 56 nucleons (26 of those are protons) and would, in the event of a collision, distribute the primary energy E_0 across all of them, the so called energy per nucleon. We already covered this in equation (4.18), but simplifying it for iron,

$$E_{\text{nuc}} = \frac{E_0}{2}\frac{m_p + m_n}{m_{\text{Fe}}} = E_0 \cdot 1.786 \times 10^{-2} = \frac{E_0}{56}, \tag{5.2}$$

uncovers that the energy is equally distributed through the nucleons. Any particles resulting from collisions of nucleons from an iron nucleus will carry energy smaller than E_{nuc}, thus an EAS will reach its maximum earlier than that of a proton primary. This is exactly what we see on longitudinal profiles from figures 5.3 and 5.4. In the case of a μBH induced EAS, however, we consider emitted μBH particles as secondary particles in an EAS and they do not posses such an even distribution

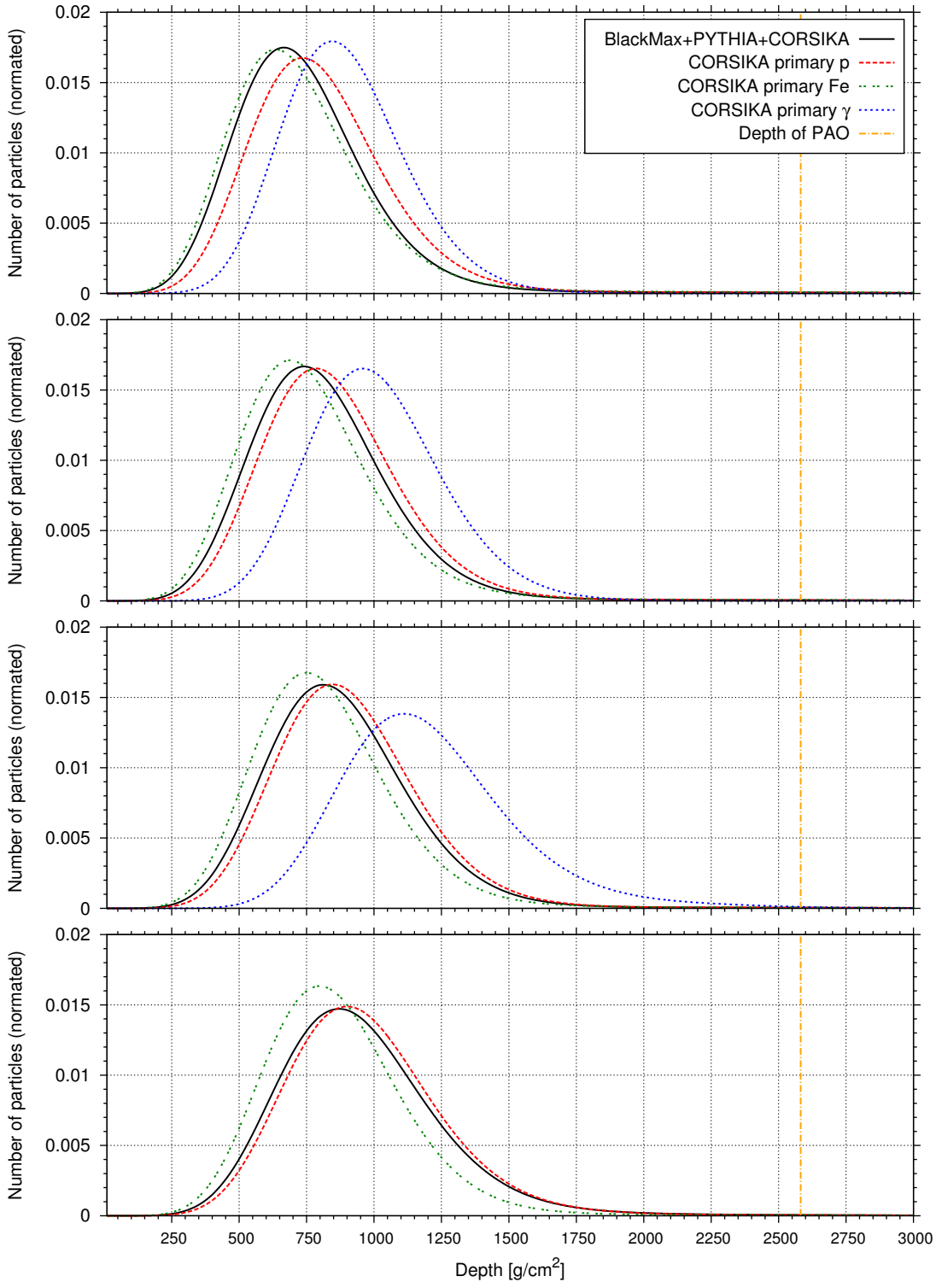

Figure 5.3: Longitudinal profiles for charged particles at inclination $\theta = 70°$ and at energies 10^{18} eV (first from top), 10^{19} eV (second from top), 10^{20} eV (third from top) and 10^{21} eV (bottom). Each set includes results from EAS using four different starting situations, a μBH induced shower and an EAS induced by primary proton, photon and iron. The profiles are normated to the total number of particles. CORSIKA limits primary photons below $E_0 = 10^{21}$ eV and there are three missing runs at energy $E_0 = 10^{20}$ eV due to a non–convergent fit.

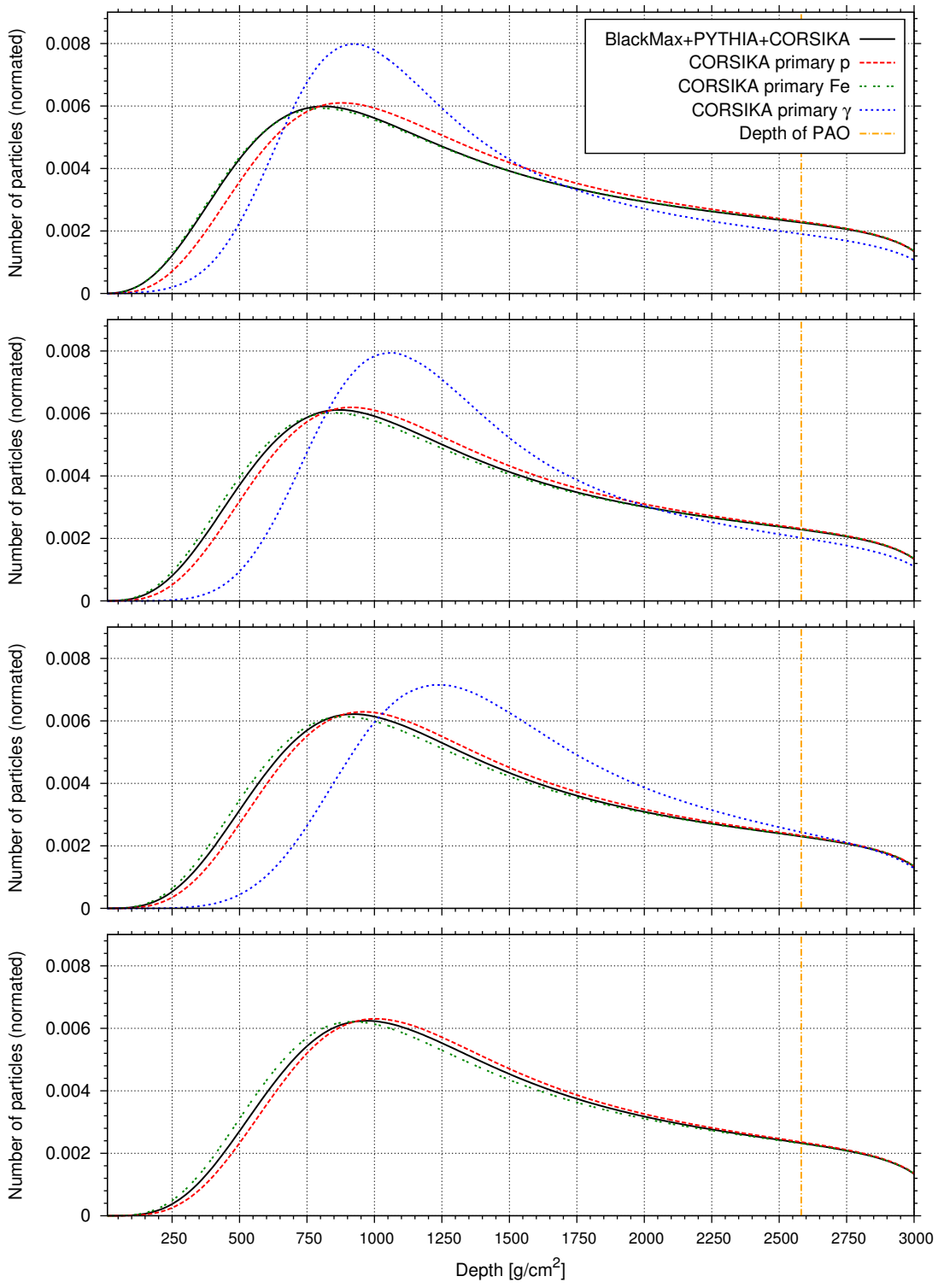

Figure 5.4: Longitudinal profiles for muons ($\mu^{\mp}$) at inclination $\theta = 70°$ and at energies 10^{18} eV (first from top), 10^{19} eV (second from top), 10^{20} eV (third from top) and 10^{21} eV (bottom). Each set includes results from EAS using four different starting situations, a μBH induced shower and an EAS induced by primary proton, photon and iron. The profiles are normated to the total number of particles. CORSIKA limits primary photons below $E_0 = 10^{21}$ eV and there are three missing runs at energy $E_0 = 10^{20}$ eV due to a non–convergent fit.

of energy. In the case of a starting collision energy $E_0 = 10^{21}$ eV, histograms on figure 5.5 show the distribution of energy across particle types The majority of

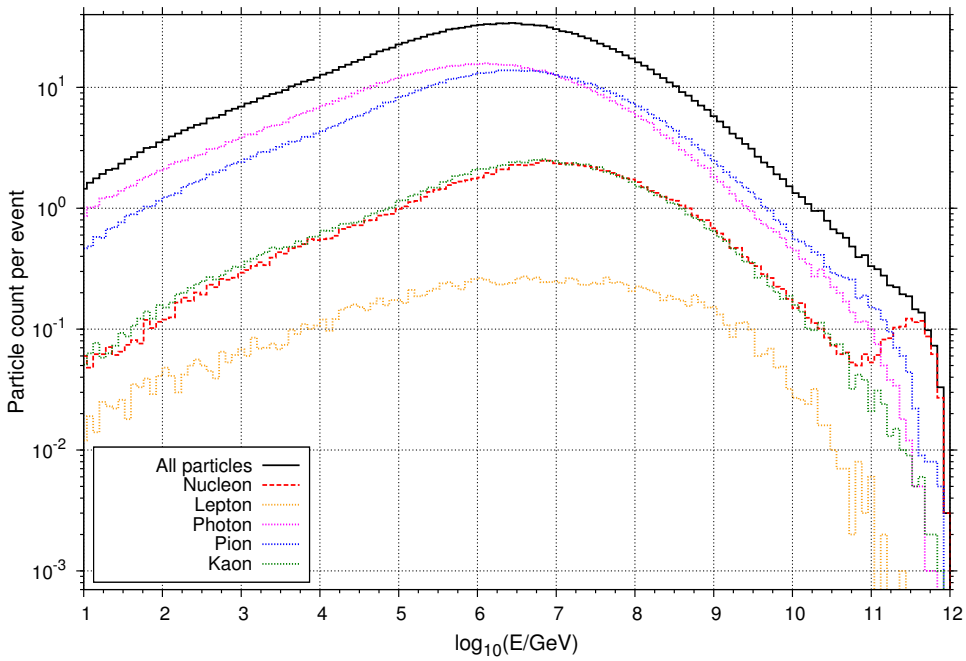

Figure 5.5: Energy histograms of particles taken after BlackMax+PYTHIA treatment and before using them with stack input to CORSIKA at energy $E_0 = 10^{21}$ eV $= 10^{12}$ GeV. The solid line represents all particles, while dotted and dashed lines arrange particles into groups (nucleons, leptons, photons, pions and kaons). No other stable particles are emitted from a μBH. The overall shape of energy histograms remains unchanged, when changing starting collision energy E_0. The number of produced μBHs was increased to 1000 events.

high–energy particles are thus nucleons that will always have energies lower than that of the initial colliding proton. In this sense, the energy distribution will be close to a primary proton, but having multiple projectiles still means an EAS will reach its maximum earlier. The reason for the shift between iron–like and proton–like EAS is, in our opinion, dependent on the particle type fraction compared to all μBH emitted particles and the energy these particles carry, compared to the available energy E_0. Figure 5.6 explains this visually by taking the sum of energies per particle type and creating an energy sum fraction (ESF) normated to the total sum of particle energies

$$\mathrm{ESF} = \frac{\sum_i E_i}{\sum_k \sum_i E_{i,k}}, \tag{5.3}$$

where i denotes a single particle from chosen particle groups and a sum over k gathers all particle groups together (creating a total sum of particle energies). The most apparent feature of figure 5.6, not considering the lepton case, is the fractions of nucleons and pions. Nucleons, more or less, constitute the whole high–energy part, and their energy fraction increases with primary energy E_0, whereas the energy fraction of pions is slightly slanted downwards, with only a small amount of

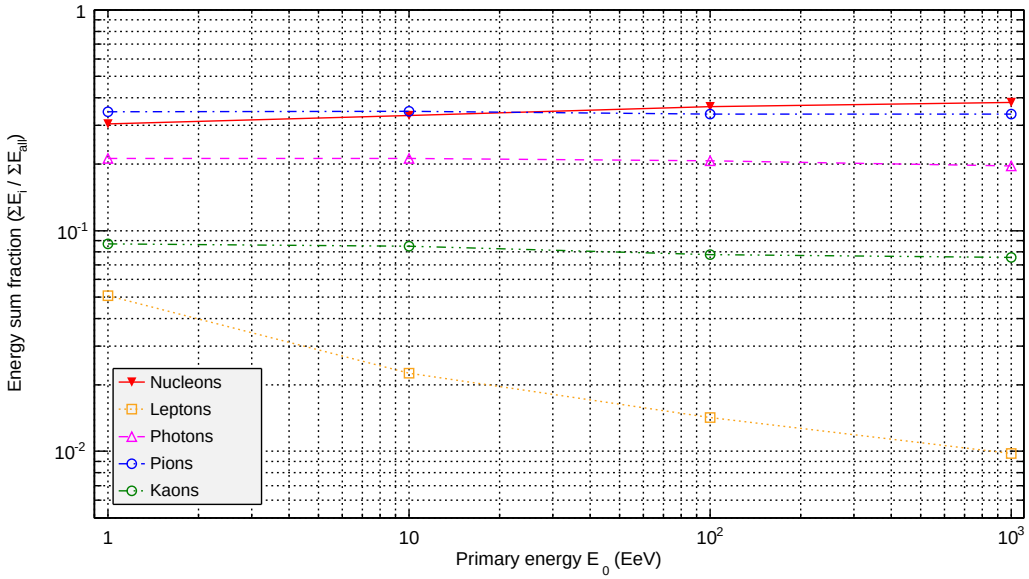

Figure 5.6: This plot represents the amount of energy distributed amongst all particle groups after BlackMax+PYTHIA treatment. The energy sum fraction is calculated as a fraction of the sum of energies from particles in one group and the total energy sum, explained in equation (5.3). The number of produced μBHs was increased to 1000 events.

high–energy candidates. This tells us that the majority of energy from pions comes from the mid–energy peak, roughly around $\sim 10^7\,\mathrm{GeV} = 10^{16}\,\mathrm{eV}$, whereas nucleons get the most notable part of energy from the high–energy peak. Connecting it to section 4.3.2, it is now simple to understand why selecting only the highest–energy particles does not change $X_{\max}$ considerably, since the bulk of these particles are in fact nucleons. Looking at figure 5.6 also reveals that, with increasing primary energy E_0, the energy fraction of nucleons increases, gradually extending the depth to shower maximum and bringing such an EAS closer to one with a starting proton primary.

A great way of comparing shower maxima for different situations of starting conditions is to directly plot $X_{\max}$ in terms of primary particle energy E_0. This way of presenting slight changes to $X_{\max}$ is more appropriate and clearer than plotting longitudinal profiles. However, we still decided to include longitudinal profile figures 5.3 and 5.4, as they show the complete evolution of a shower. Gathering longitudinal profiles from these plots and fitting their longitudinal profile data using the Gaisser–Hillas function (5.1), enabled us to present $X_{\max}$ in greater detail on figures 5.7 and 5.8. The first figure shows shower maxima for profiles of charged particles, while the second displays those of only muons. This separation is useful, because our detectors detect charged particles, from which muons are most likely to reach ground–based detectors in inclined showers. Again, it is important to note the shift of $X_{\max}$ for μBH induced EAS on both plots and the relatively constant separation between showers with proton and iron primaries. The rate of evolution of $X_{\max}$ with energy, known as elongation rate, of both proton and iron induced EAS are comparable. The same can not be said for showers with intermediate μBHs producing a completely unique elongation rate, most notable at low primary energy E_0 values.

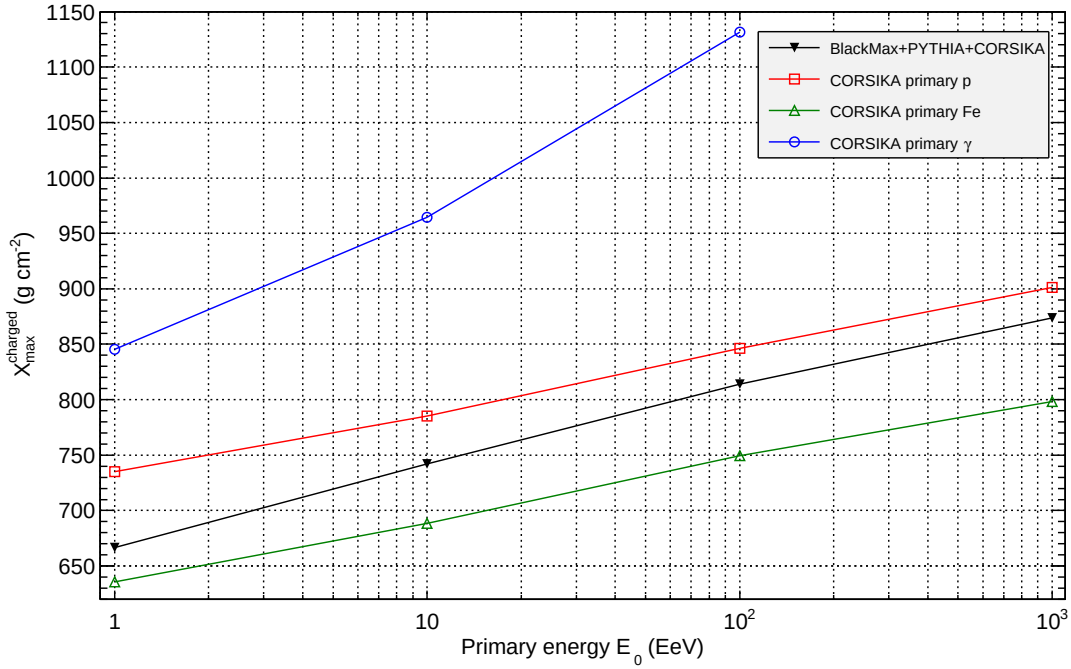

Figure 5.7: Shower maxima $X_{\max}^{\text{charged}}$ for the four starting situations obtained by fitting each longitudinal profile from a set of 100 showers (their average profile is shown in figure 5.3) with function (5.1).

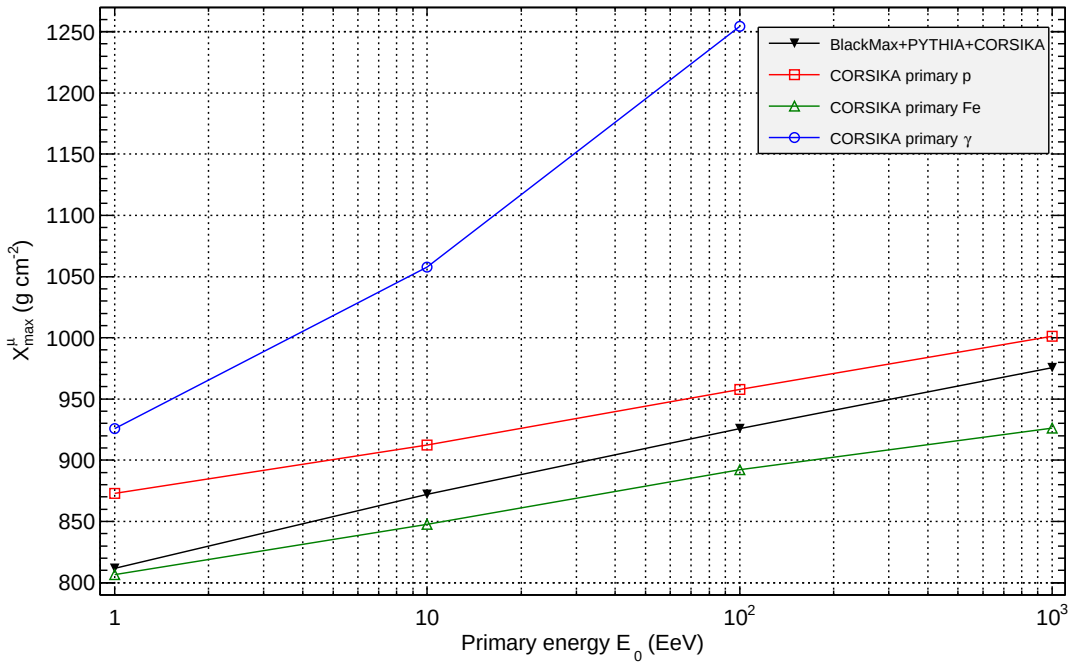

Figure 5.8: Shower maxima $X_{\max}^{\mu}$ for the four starting situations obtained by fitting each longitudinal profile from a set of 100 showers (their average profile is shown in figure 5.4) with function (5.1).

As a further comparison between starting situations, a good indicator to what kind of EAS we have, is to plot the muon multiplicity fraction of a shower. Simply put, the amount of muons produced in a shower is determined by muon multiplicity or integral under the muon longitudinal profile. To put this value in context, we normate it to the multiplicity of all charged particles in a shower. A muon multiplicity fraction for the four different primary types and energy ranges already used in earlier simulations is displayed on figure 5.9. Quite differently from what

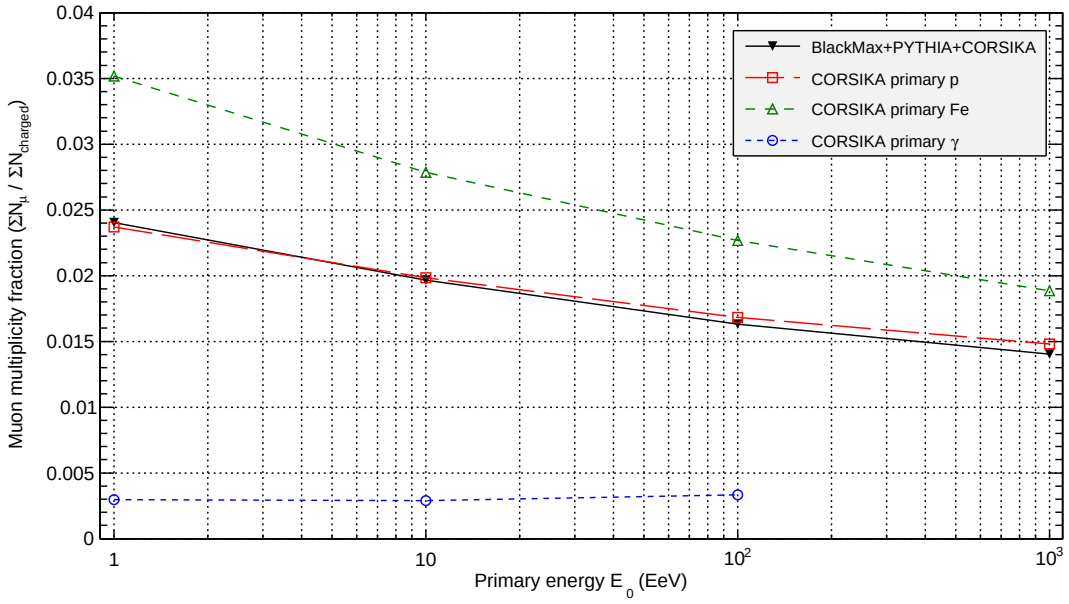

Figure 5.9: Muon multiplicity for four starting situations, including EAS with a μBH intermediate stage, proton, photon and iron primaries. Multiplicities were normated to the number of all charged particles produced in each shower profile.

we see on $X_{\max}$ plots, a μBH induced shower is not between proton induced and iron induced showers, but is instead remarkably close to an EAS with a proton primary. This tells us that extensive air showers with an intermediate μBH stage behave in a similar way than normal proton induced showers, whereas iron primaries produce a larger muon fraction during shower evolution. The reason for this is that iron primaries produce a larger number of hadrons during the initial collision, consequently populating the multiplicity of muons through further interactions of charged pions (π^+, π^-). A complete outsider on figure 5.9 is a photon produced EAS, with its electromagnetic shower and unsurprisingly low muon content.
CORSIKA is equipped and can be used with a number of hadron interaction models, separately treating low and high energy shower particles. It is expected that varying models will produce some sort of difference in shower maxima. In hopes of finding additional information on μBH induced EAS, by changing how micro black hole emitted particles interact with atmospheric molecules, we decided to perform a second collection of simulations involving Epos–LHC as the high–energy hadron interaction model. Epos–LHC, just as QGSJETII-04, was updated to include data gathered at the LHC, where both of these exhibit similar cross–section values. The main difference, however, is due to extrapolated cross–sections at collision energies above that of current experimental values from accelerators. An in–depth compar-

ison of both models including LHC data is presented in [37], describing the large difference between models at ultra high energies. For UHECR, the two models will undoubtedly produce unmatching results, but performing simulations using both offers us the extent of flexibility that we are facing in determining $X_{\max}$ values. As before, we split simulation runs according to primary energy E_0 and primary particle type, while keeping parameters constant, as well as the low–energy hadron interaction model (FLUKA). The process of fitting longitudinal profile data was the same as in previous simulations. Figure 5.10 compares shower maxima for muons $X^{\mu}_{\max}$ of EAS using either QGSJETII–04 (solid line) or Epos–LHC (dashed line) interaction models. Examining the difference between the two models, it quickly becomes apparent that Epos–LHC, in general, produces showers with a deeper shower maximum, ranging from a nearly equal $X_{\max}$ value to as much as $25\,\mathrm{g\,cm^{-2}}$ increase at highest energies. On the other hand, the large shift in $X_{\max}$ for proton primaries at 10 EeV seems inconsistent with remaining proton data points and could be the result of low statistics. It is apparent that this produces a restriction on how well we can determine shower maxima from a small collection of simulations used for this thesis (100 simulated showers). The errors we are most likely producing, when using such a small dataset, amounts to at least $10\,\mathrm{g\,cm^{-2}}$, although individual fitting errors on average $X_{\max}$ are below $2\,\mathrm{g\,cm^{-2}}$. Despite these inconsistencies and changes between the models, it is nonetheless important to notice that the behavior, concerning primary particle types, remains more or less the same. Shower maxima of μBH induced EAS still resemble iron induced showers at low energies and switch to a more proton–like EAS at higher energies, no matter which model we choose.

The information currently gathered by the Pierre Auger Observatory is displayed in figure 5.11, serving as a comparison to our own simulation results in figure 5.10. The two plots have different shower inclinations, most notably seen in the ranges of $X^{\mu}_{\max}$ values. If a direct comparison is needed, then equation (4.10) can be used to transform them to vertical depth. Either way, relative separations between starting particle cases and high–energy hadron interaction models can still be taken into consideration. Epos–LHC model has larger values of $X_{\max}$ on both figures and the rate of evolution of $X_{\max}$ for iron and proton regarding both models is approximately equal. The fundamental difference, however, is in the behavior of PAO data points and the way μBH induced shower simulation data points change with energy. In the first case, data points seem to converge from a proton–like EAS at lower energies to $X_{\max}$ values similar to an iron induced EAS, while in the μBH case it is just the opposite. Current observed values thus contradict the possibility of detecting μBH induced extensive air showers, using the calculation of first interaction depth equal to that of protons.

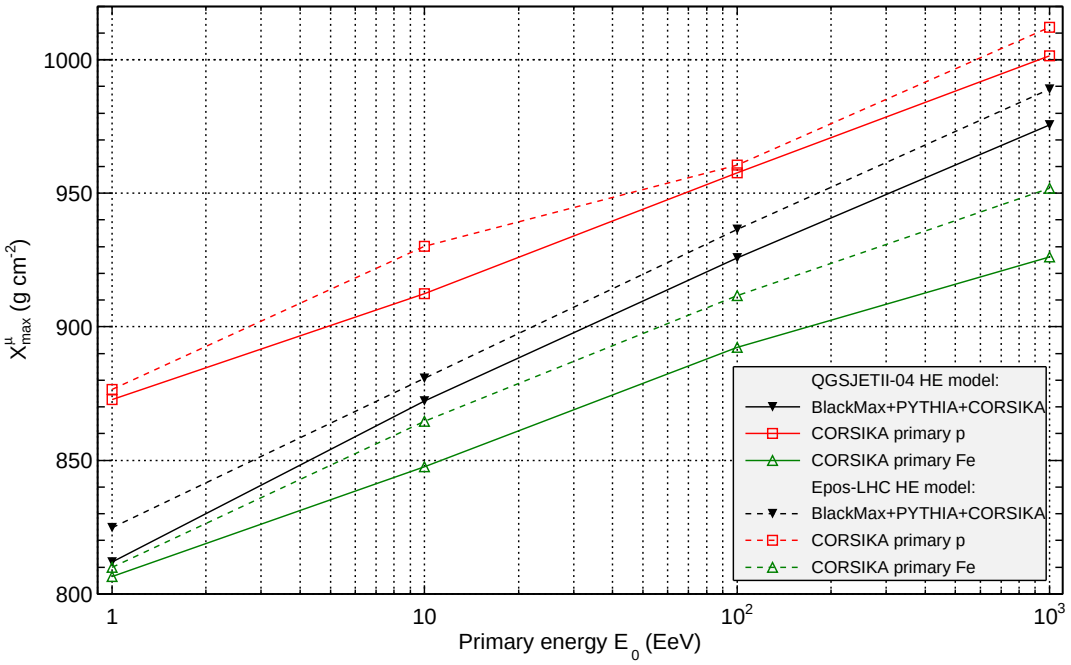

Figure 5.10: Comparing muon shower maxima $X^{\mu}_{\max}$ for two high–energy interaction models, QGSJETII–04 (solid line) and Epos–LHC (dashed line). Since photons have an electromagnetic EAS, only μBH, proton and iron induced shower are displayed. One proton primary EAS simulation at energy $E_0 = 10^{21}$ eV was discarded, due to a nonconvergent fit.

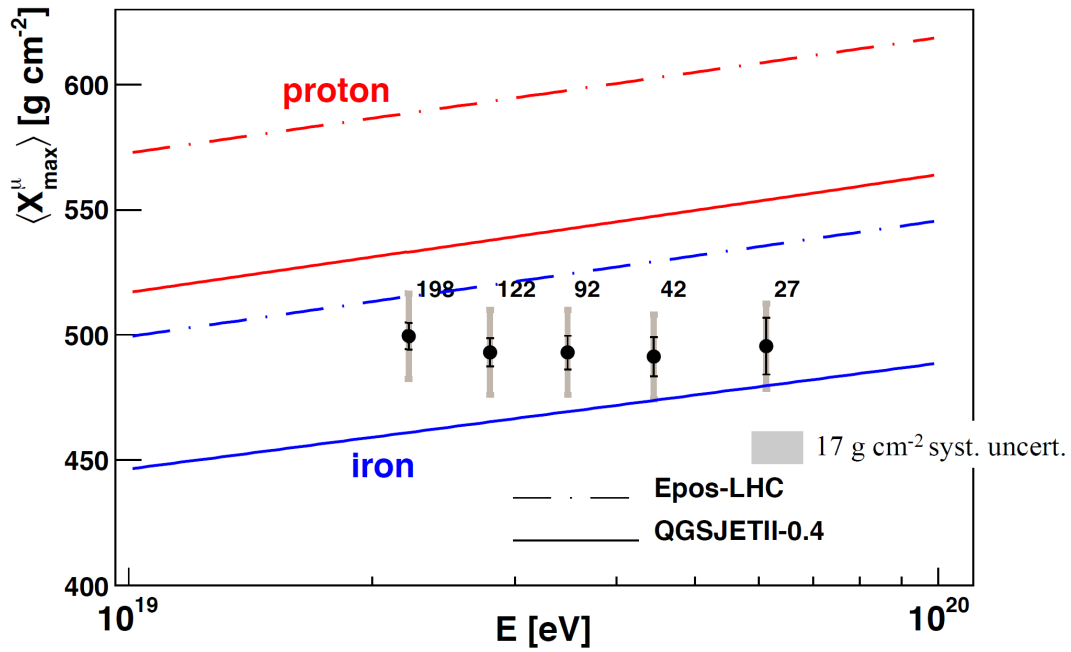

Figure 5.11: Pierre Auger observatory results (black dots with error bars and numbers, indicating the number of selected data in each energy bin), compared to simulations using two high–energy interaction models (Epos–LHC and QGSJETII–04) and two primary particle types (proton and iron). Primary particle inclination angle is limited between 55° and 65° (figure ref. [38]).

6 Conclusions and future prospects

The possibility of distinguishing a μBH induced EAS was in this thesis investigated with the use of three simulators — BlackMax, PYTHIA and CORSIKA. Each covered a part of the complete simulation process, where the connection between BlackMax/PYTHIA and CORSIKA was only a listing of stable particles exiting the μBH evaporation with a subsequent treatment of parton showers, photon showers, particle decays and hadronization performed by PYTHIA. Adaptations of simulators are described in chapters 4.2, 4.3.2 and 4.3.3, involving:

- a custom histograming function, instead of the normal BlackMax, BlackMax+PYTHIA or BlackMax+HERWIG particle output,
- an increase to the amount of particle holders for a complete treatment in PYTHIA or HERWIG,
- updates of particle masses in PYTHIA and HERWIG to those from the PDG,
- transformation of particles from the laboratory to the center–of–mass frame for their use in CORSIKA,
- a random first interaction depth calculation for CORSIKA with stack input option enabled.

With all Monte Carlo simulators ready, simulations were separated into sets of four UHECR energies, from 10^{18} eV to 10^{21} eV and steps of one order of magnitude. Each of these sets consisted of four independent starting conditions. One was a μBH induced EAS, while the rest had primary proton, iron and photon particles, respectively. After performing a fit to the longitudinal shower profile data and analyzing the maximum value $X_{\max}$ for all charged particles and muons, results show that a μBH started shower resides somewhere between a proton induced shower and an iron induced shower. There is also a trend that shifts $X_{\max}$ of the μBH case from the iron one at lower energies, towards a more proton–like case at higher energies, most likely attributed to the energy distribution amongst μBH emitted particles.

We must stress that the performed simulations do not account for a far smaller micro black hole production cross section (a geometrical cross section given as an estimate), with a difference of roughly 6 to 7 orders of magnitude, compared to the proton–air collision cross section. Expectedly, using such a small cross section when running a CORSIKA simulation returns first interaction depth far larger than the depth attributed to the sea level, thus not even producing an EAS. Repeating simulations for a large number of times, would most likely give a valid first interaction depth, but realistically speaking, observing a μBH induced shower would be severely suppressed by the far greater number of normal showers. This further transcends from simulations to the observational aspect of UHECR, where an extremely large set of such high–energy shower events would have to be observed, a difficulty due to the low flux at the high–energy end of the cosmic ray spectrum.

Another argument against the possibility of detecting μBHs through EAS, comes

from the randomness of arrival directions of UHECR and the long–standing question of their particle structure. As of yet, we are not able to say if such particles are protons, iron or something completely different. This in turn means that μBH induced showers that possibly have longitudinal profile maxima somewhere between the two, are not unique enough to separate their showers at this moment. However, with development of new detector systems, the possibility to detect small differences between $X_{\max}$ could give some identity to the primary particle.
For any future work regarding simulations of μBH induced EAS, some issues and additional considerations have to be addressed:

1. The linking process described in this thesis between BlackMax and CORSIKA is not ideal, as both programs are run separately. Ideally, the two programs should be interconnected, making it possible to inject input particles to CORSIKA on the fly and reduce the amount of data needed to upload and download for GRID simulations.

2. 100 events from BlackMax, corresponding to 100 showers from CORSIKA, produce a limited dataset. Therefore, larger statistics have to be acquired by running additional simulations.

3. With a high multiplicity of simulations, μBH formation cross–section needs to be accounted for when calculating first interaction depth in CORSIKA.

4. Cosmic rays that do not form a μBH (impact parameter is too large) should, for an even more accurate description of the formation of air showers, produce a normal EAS. Such *missed* events are possible, but filtered out in BlackMax, since the purpose of the program is to create μBH events.

5. BlackMax assumes a collision between two protons, while in cosmic rays the collision is between a primary particle and an air molecule. This does not change the actual collision (which is on the parton level), but there is a change in cross section and the number of partons immediately after the collision.

A possible direction for future work in detection of μBH induced EAS is to take a closer look at horizontal showers, where collisions between neutrinos with extreme energies and air molecules form a μBH, assuming neutrinos with extreme energies exist. This kind of research would include the μBH formation cross–section, producing a shower deeper in the atmosphere named a *young shower*. As opposed to horizontal hadron showers or *old showers*, where only muons arrive to the detector, *young showers* develop their electro–magnetic part of the shower close enough to the detector for it to detect EM particles other than muons. Simulations, similar to those presented in this thesis, can then be used to investigate differences between a horizontal neutrino shower and a μBH induced horizontal shower (with a neutrino starting particle). If *young showers* are uncovered though experimental work, we can prove the existence of neutrinos with extreme energies and possibly even the existence of μBHs. Otherwise, we will at least get a limit on μBH cross–section or some of the model specific μBH free parameters.

Appendix A: Conversion factors and constants

In this thesis, as it is common for astroparticle physics purposes, energies are given in units of electron–volt

$$1\,\mathrm{eV} = 1\,\frac{\mathrm{J}}{\mathrm{C}} \cdot q_0 = 1.602176565(35) \times 10^{-19}\,\mathrm{J}, \tag{1}$$

where q_0 is the elementary charge. Unfortunately, we are dealing with a large range of energies and it is therefore important to use SI prefixes that best describe the range of energies we are presenting. A table of prefixes and the conversion factors to base units can be seen in table 1.

Table 1: SI prefix names and conversions to base units used throughout this thesis.

Prefix	Conversion to base	Prefix	Conversion to base
exa (E)	10^{18}	kilo (k)	10^{3}
peta (P)	10^{15}	mili (m)	10^{-3}
tera (T)	10^{12}	micro (μ)	10^{-6}
giga (G)	10^{9}	nano (n)	10^{-9}
mega (M)	10^{6}	pico (p)	10^{-12}

All constants that appear in equations have their values in table 2.

Table 2: Constants used in equations appearing in this thesis [28].

Quantity	Value
gravitational constant (G)	$6.67384(80) \times 10^{-11}\,\mathrm{m^3\,kg^{-1}\,s^{-2}}$
speed of light (c)	$299792458\,\mathrm{m\,s^{-1}}$
reduced Planck constant ($\hbar$)	$1.054571726(47) \times 10^{-34}\,\mathrm{J\,s} =$ $= 6.58211928(15) \times 10^{-16}\,\mathrm{eV\,s}$
solar mass ($M_\odot$)	$1.9885(2) \times 10^{30}\,\mathrm{kg}$
Boltzmann constant (k_B)	$1.3806488(13) \times 10^{-23}\,\mathrm{J\,K^{-1}}$
Avogadro constant (N_A)	$6.02214129(27) \times 10^{23}\,\mathrm{mol^{-1}}$
Elementary charge (q_0)	$1.602176565(35) \times 10^{-19}\,\mathrm{C}$

Sometimes it's beneficial to present quantities in natural units in order to reduce or completely remove constants such as the speed of light c, the Planck $\hbar$ and Boltzmann k_B constants. In this case, we can set $\hbar = c = k_B = 1$. There is a possibility to convert between SI units and natural units with conversion factors listed in table 3. This table is used by choosing the quantity and for

the specified conversion, multiplying the quantity with the conversion factor. For reverse conversions, we need to divide the quantity with the conversion factor. As an example, if we wish to find out the mass of a proton ($m_p = 1.672622 \times 10^{-27}\,\mathrm{kg}$) in natural units of GeV, we only need to take the factor c^{-2} from the table and divide proton mass with it

$$m_p = \frac{1.672621 \times 10^{-27}\,\mathrm{kg}}{c^{-2}} = \frac{1.672622 \times 10^{-27}\,\mathrm{kg}}{1.782662 \times 10^{-27}\,\mathrm{GeV^{-1}\,kg}} = 0.938272\,\mathrm{GeV}.$$

However, when trying to convert more complex units into natural units, we need to make sure to exclude any c, $\hbar$ or k_B constants to correctly use them in equations. For example, in the Schwarzschild radius formula (3.2), we can convert the gravitational constant to units of $\mathrm{m\,GeV^{-1}}$, so the mass can directly be inserted in units of electron–volts. In natural units, the equation would lose the speed of light constant and become just

$$r_s = 2GM,$$

where G no longer has units of $\mathrm{m^3\,kg^{-1}\,s^{-2}}$ as seen in table 2, but $\mathrm{m\,kg^{-1}}$ due to losing units coming from c^2. Therefore, we only need to take the conversion factor for mass to achieve our desired initial conversion

$$\begin{aligned} G =& 6.67384 \times 10^{-11}\,\mathrm{m\,kg^{-1}} \cdot 1.782662 \times 10^{-27}\,\mathrm{GeV^{-1}\,kg} = \\ =& 1.189720 \times 10^{-37}\,\mathrm{m\,GeV^{-1}}. \end{aligned}$$

Table 3: Conversion factors between SI units and natural units.

Quantity	Conversion	Factor
time (t)	$\mathrm{GeV^{-1}} \Rightarrow \mathrm{s}$	$\hbar = 6.58211928 \times 10^{-25}\,\mathrm{GeV\,s}$
length (l)	$\mathrm{GeV^{-1}} \Rightarrow \mathrm{m}$	$\hbar c = 1.973269718 \times 10^{-16}\,\mathrm{GeV\,m}$
cross–section (σ)	$\mathrm{GeV^{-2}} \Rightarrow \mathrm{mb}$	$(\hbar c)^2 = 0.389379338\,\mathrm{GeV^2\,mb}$
mass (m)	$\mathrm{GeV} \Rightarrow \mathrm{kg}$	$c^{-2} = 1.782662 \times 10^{-27}\,\mathrm{GeV^{-1}\,kg}$
temperature (T)	$\mathrm{GeV} \Rightarrow \mathrm{K}$	$k_B^{-1} = 1.160452 \times 10^{13}\,\mathrm{GeV^{-1}\,K}$

Appendix B: Particle codes for stack input

CORSIKA has a different way of ordering particles into particle codes than the standard Monte Carlo numbering scheme given by PDG [28]. Furthermore, not all of the particles inside the CORSIKA numbering scheme can be used with the stack input option. For this purpose, table 4 lists all particles that can be used with stack input and at the same time compares both numbering schemes (for easier transformation between them).

Table 4: All particles that can be used with CORSIKA stack input, with added numbering schemes from CORSIKA and PDG [28].

Particle	CORSIKA	PDG	Particle	CORSIKA	PDG
γ	1	22	$\overline{\Sigma}^0$	28	−3212
e^+	2	−11	$\overline{\Sigma}^+$	29	−3222
e^-	3	11	$\overline{\Xi}^0$	30	−3322
μ^+	5	−13	$\overline{\Xi}^+$	31	−3212
μ^-	6	13	$\overline{\Omega}^+$	32	−3334
π^0	7	111	ω	50	223
π^+	8	211	ρ^0	51	113
π^-	9	−211	ρ^+	52	213
K^0_L	10	130	ρ^-	53	−213
K^+	11	321	Δ^{++}	54	2224
K^-	12	−321	Δ^+	55	2214
n	13	2112	Δ^0	56	2114
p	14	2212	Δ^-	57	1114
$\overline{p}$	15	−2212	$\overline{\Delta}^{--}$	58	−2224
K^0_S	16	310	$\overline{\Delta}^-$	59	−2214
η	17	221	$\overline{\Delta}^0$	60	−2114
Λ	18	3122	$\overline{\Delta}^+$	61	−1114
Σ^+	19	3222	K^{*0}	62	313
Σ^0	20	3212	K^{*+}	63	323
Σ^-	21	3112	K^{*-}	64	−323
Ξ^0	22	3322	$\overline{K^*}^0$	65	−313
Ξ^-	23	3312	ν_e	66	12
Ω^-	24	3334	$\overline{\nu}_e$	67	−12
$\overline{n}$	25	−2112	ν_μ	68	14
$\overline{\Lambda}$	26	−3122	$\overline{\nu}_\mu$	69	−14
$\overline{\Sigma}^-$	27	−3112			

Bibliography

[1] T.K. Gaisser, T. Stanev, S. Tilav, *Cosmic ray energy spectrum from measurements of air showers*, Frontiers of Physics Vol. 8, **6** (2013), 748 – 758, arXiv:1303.3565v1.

[2] M.S. Longair, *High Energy Astrophysics (3rd edition)*, Cambridge University Press (2011).

[3] http://www.lip.pt/~jespada/Research/develop.jpg, (9.3.2014).

[4] http://physics.aps.org/assets/f842dc5c-a38c-4a5b-b1f5-d042e072079a, (11.3.2014).

[5] http://scienceblogs.com/startswithabang/files/2013/02/Hawking-Radiation_02.jpeg, (11.3.2014).

[6] http://jameswharris.files.wordpress.com/2014/02/planck_scale.gif, (14.3.2014).

[7] http://www.faculty.umb.edu/gary_zabel/Courses/Parallel%20Universes/Images/Eras-universe-031.jpg, (14.3.2014).

[8] N. Arkani–Hamed, S. Dimopoulos, G. Dvali, *The hierarchy problem and new dimensions at a millimeter*, Phys. Lett. B, **396** (1998), 263 – 272, arXiv:hep-ph/9803315v1.

[9] http://th.physik.uni-frankfurt.de/~hossi/Bilder/gravweg2.jpg, (14.3.2014).

[10] F.R. Tangherlini, Nuovo Cimento **27** (1963) 636 – 651.

[11] R.C. Myers, M.J. Perry, *Black holes in higher dimensional space–times*, Ann. Physics **172** (1986) 304 – 347.

[12] S.C. Park, *Black holes and the LHC: A review*, Progress in particle and nuclear physics **67** (2012) 617 – 650.

[13] http://th.physik.uni-frankfurt.de/~hossi/Physics/Bummbunt.jpg, (4.4.2014).

[14] J.P. Ottersbach, *Micro black holes at the LHC*, Diploma thesis, http://www.atlas.uni-wuppertal.de/diplom/WUD07-10_john_p_ottersbach.pdf.

[15] The CMS Collaboration, *Search for microscopic black holes in pp collisions at* $\sqrt{s} = 7\ TeV$, J. High Energy Phys. **04** (2012) 061, arXiv:1202.6396v2 [hep-ex].

[16] The CMS Collaboration, *Search for microscopic black holes in pp collisions at* $\sqrt{s} = 8\ TeV$, J. High Energy Phys. **07** (2013) 178, arXiv:1303.5338v2 [hep-ex].

[17] The ATLAS collaboration, *Search for strong gravity signatures in same–sign dimuon final states using the ATLAS detector at the LHC*, Phys. Lett. B **709** (2012) 322 – 340, arXiv:1111.0080v2 [hep-ex].

[18] C.M. Harris, P. Richardson, B.R. Webber, *CHARYBDIS: A black hole event generator*, J. High Energy Phys. **08** (2003) 033.

[19] D.–C. Dai *et al.*, *BlackMax: A black–hole event generator with rotation, recoil, split branes and brane tension*, Phys. Rev. D **77** (2008) 076007.

[20] J.A. Frost *et al.*, *Phenomenology of Production and Decay of Spinning Extra–Dimensional Black Holes at Hadron Colliders*, arXiv:0904.0979v4 (16.10.2009).

[21] T. Sjöstrand *et al.*, *PYTHIA 6.4 physics and manual*, J. High Energy Phys. **05** (2006) 026.

[22] G. Corcella *et al.*, *HERWIG 6.5*, J. High Energy Phys. **0101** (2001) 010.

[23] D. Heck *et al.*, *Report FZKA* **6019** (1998).

[24] M.R. Whalley, D. Bourilkov, R.C. Group, *The Les Houches accord PDFs (LHAPDF) and LHAGLUE*, arXiv:hep-ph/0508110 (9.8.2005).

[25] G.B. Yodh *et al.*, *Proton–proton cross sections from* 1 *to* 100 *TeV*, Phys. Rev. D **27** (1983) 1183 – 1186.

[26] D.–C. Dai *et al.*, *The BlackMax Manual, Version 2.00*, arXiv:0902.3577 (20.2.2009).

[27] J. Alwall *et al.*, *A standard format for Les Houches Event files*, arXiv:hep-ph/0609017v1 (3.9.2006).

[28] J. Beringer *et al.*, Review of particle physics (Particle Data Group), Phys. Rev. D **86** (2012) 010001.

[29] A. Ferrari *et al.*, *FLUKA: A multi–particle transport code*, CERN 2005–10 (2005), INFN/TC_05/11, SLAC–R–773.

[30] G. Battistoni *et al.*, *The FLUKA code: Description and benchmarking*, Proceedings of the Hadronic Shower Simulation Workshop 2006, Fermilab 6–8 September 2006, M. Albrow, R. Raja eds., AIP Conference Proceedings 896, 31–49, (2007).

[31] S. Ostapchenko, *Monte Carlo treatment of hadronic interactions in enhanced Pomeron scheme: QGSJET-II model*, Phys. Rev. D **83** (2011) 014018.

[32] T. Pierog, Iu. Karpenko, J.M. Katzy, E. Yatsenko, K. Werner, *EPOS LHC: test of collective hadronization with LHC data*, arXiv:1306.0121v2 (20.12.2013).

[33] D. Heck, J. Knapp, Report **FZKA 6097** (1998), Forschungszentrum Karlsruhe, https://web.ikp.kit.edu/heck/publications/fzka6097.pdf.

[34] D. Heck, T. Pierog, *Extensive Air Shower Simulation with CORSIKA: A User's Guide*, http://www-ik.fzk.de/~corsika/usersguide/usersguide.pdf, (3.9.2013).

[35] Geomag, http://www.ngdc.noaa.gov/geomag-web/#igrfwmm, (29.1.2014).

[36] T.K. Gaisser, A.M. Hillas, Proc. 15th Int. Cosmic Ray Conf. (Plovdiv) **8** (1977) 353 – 357.

[37] T. Pierog, J. Phys.: Conf. Ser. **409** (2013) 012008.

[38] D. García–Gámez for the Pierre Auger Collaboration, 33rd Int. Cosmic Ray Conf. (ICRC2013) 40 – 43, arXiv:1307.5059.